Septin Filament Compaction Into Rings Requires the Anillin Mid2 and Contractile Ring Constriction

Federica Arbizzani, Manos Mavrakis, Marta Hoya, Juan Carlos Ribas, Sophie Brasselet, Anne Paoletti, Sergio Rincon

Septin filament compaction into rings requires the anillin Mid2 and contractile ring constriction

Federica Arbizzani[1], Manos Mavrakis[2+], Marta Hoya[3+], Juan Carlos Ribas[3], Sophie Brasselet[2], Anne Paoletti[1]* and Sergio A. Rincon[3]*

Running title: Mid2 promotes fission yeast septin ring assembly

[1] Institut Curie, PSL University, CNRS UMR 144, F-75005, Paris, France.

[2] Aix Marseille Université, CNRS, Centrale Marseille, Institut Fresnel, UMR 7249, Marseille, France.

[3] Instituto de Biología Funcional y Genómica and Departamento de Microbiología y Genética, Consejo Superior de Investigaciones Científicas (CSIC) / Universidad de Salamanca, Salamanca, 37007 Spain.

*corresponding authors and equal contribution

+ equally contributing authors

Correspondance: anne.paoletti@curie.fr and sarpadilla@usal.es

SUMMARY

Septin filaments assemble into high-order molecular structures that associate with membranes, acting as diffusion barriers and scaffold proteins crucial for many cellular processes. However, how septin filaments organize in such structures is still not well understood. In this study, we used fission yeast to explore septin filament organization during cell division and decipher key factors responsible for their regulation. Live-imaging and polarization microscopy analysis uncovered that septin filaments are initially recruited as a diffuse meshwork surrounding the acto-myosin contractile ring (CR) in anaphase, which undergoes compaction into two rings when CR constriction is initiated. We found evidence that the anillin-like protein Mid2 is necessary to promote this novel compaction step, possibly acting as a bundler for septin filaments. We also found that Mid2-driven septin compaction requires inputs from the Septation Initiation Network (SIN) as well as CR constriction or the β(1,3)-glucan synthase Bgs1. This work highlights the complex regulations that allow the coordination between septin ring assembly and cell cycle progression.

INTRODUCTION

Cytokinesis is an irreversible process which must precisely partition an equal set of the replicated chromosomes and organelles into each daughter cell. Defects in this process can lead to chromosome mis-segregation or aneuploidy, a hallmark of cancer (Storchova and Pellman, 2004; Fujiwara et al., 2005; Lacroix and Maddox, 2012). Cytokinesis completion requires the participation of different components of the cytoskeleton, namely, the actin cytoskeleton at the basis of the contractile ring (CR) that pinches in the plasma membrane to create the cleavage furrow, microtubules involved in division plane signaling in animal cells, as well as septins which are present at the division site from yeast to mammals.

Septins are unique cytoskeletal components capable of self-assembling to form high-order molecular structures of varied shapes such as filaments and rings. Their ability to interact with cellular membranes through interaction with negatively charged phospholipids, such as phosphatidylinositol 4,5-bisphosphate (PIP2) as well as with actin filaments and microtubules allows them to participate in many biological processes, working as diffusion barriers for protein compartmentalization and/or scaffolds for protein-protein interactions (Bertin et al., 2010; Saarikangas and Barral, 2011; Mostowy and Cossart, 2012; Bridges et al., 2014; Bridges and Gladfelter, 2015; Bridges et al., 2016; Marquardt et al., 2019). These conserved GTP-binding proteins were initially discovered in budding yeast, based on their role in cytokinesis, a function which was found to be conserved in animals (Hartwell, 1971; Neufeld and Rubin, 1994; Gladfelter et al., 2001; Surka et al., 2002; Kozubowski et al., 2005; Versele and Thorner, 2005; McMurray and Thorner, 2009; Estey et al., 2010; Wu et al., 2010; Kim et al., 2011; Kechad et al., 2012; El Amine et al., 2013; Founounou et al., 2013; Cauvin and Echard, 2015). Importantly, septins in budding yeast serve as a scaffold for the sequential and ordered assembly of the acto-myosin based CR (Juanes and Piatti, 2016; Meitinger and Palani, 2016; Bhavsar-Jog and Bi, 2017). Later on, when CR constriction occurs, septins act as cortical barriers to create specialized confined zones at the cleavage furrow where membrane reorganization and septum formation happen during cell division (Dobbelaere and Barral, 2004).

In budding yeast septin organization undergoes multiple transitions during the cell cycle. In early G1, septins initially assemble as a patch-like structure at the presumptive bud site. Upon bud emergence, this patch narrows to form a single ring marking the site of bud growth. Once the bud has formed, the septin ring extends into an hourglass-shaped collar present at the mother-bud neck until mitotic entry. At cytokinesis onset, the septin hourglass splits into two distinct rings that sandwich the CR (Gladfelter et al., 2001). Finally, after cell division, the septin rings disassemble and the septin subunits are recycled for a new cycle to begin (McMurray and Thorner, 2009).

One important factor in the organization of septins is the conserved protein anillin, whose disruption leads to defects in animal cytokinesis (Oegema et al., 2000; Somma et al., 2002; Echard et al., 2004; Field et al., 2005; Straight et al., 2005; Zhao and Fang, 2005; Hickson and O'Farrell, 2008; Piekny and Glotzer, 2008). Indeed, anillin bridges septins and the CR during cell division (Oegema et al., 2000; Kinoshita et al., 2002; Field et al., 2005; Kechad et al., 2012; Liu et al., 2012). *In vitro* studies have shown that anillin can bind septin and actin filaments. Animal anillin interacts with septins and PIP2 through a C-terminal PH domain located after the anillin homology domain (Piekny and Glotzer, 2008; Piekny and Maddox, 2010; Kechad et al., 2012; Liu et al., 2012). The C-terminal region of Bud4, the anillin-like protein in budding yeast, is important to direct septin organization during bud site selection and bud growth and to preserve the integrity of the septin ring during cytokinesis (Wloka et al., 2011; Eluere et al., 2012; Kang et al., 2013; Wu et al., 2015). Thus, in *bud4Δ* mutants the septin double ring disassembles during cytokinesis (Kang et al., 2013), whereas the overexpression of Bud4 leads to the formation of extra septin structures. More recently, polarized fluorescence microscopy studies have described a key role of Bud4 in the reorientation of septin filaments in the hourglass to double ring transition (McQuilken et al., 2017).

The fission yeast *Schizosaccharomyces pombe*, a recognized model system for cytokinesis studies, is a rod-shaped organism that divides by the assembly and constriction of a medially placed actomyosin-based CR. *S. pombe* has two anillin-like proteins, Mid1 and Mid2, with non-overlapping functions (Berlin et al., 2003; Tasto et al., 2003). Mid1 accumulates at the medial cortex at mitosis onset, where it recruits components involved in CR assembly (Pollard and Wu, 2010; Lee et al., 2012; Rincon and

Paoletti, 2012; Rincon and Paoletti, 2016). CR constriction and synthesis of the septum (the extracellular cell wall separating the two daughter cells) are triggered upon mitotic exit by the SIN pathway, related to the budding yeast Mitotic Exit Network and the metazoan Hippo pathway (Hergovich et al., 2006; Cortés et al., 2016). *S. pombe* septins were identified by sequence homology with the *S. cerevisiae* counterparts (Wood et al., 2002). Spn1-4 are expressed in vegetatively growing cells and localize to the division site. However, differently from *S. cerevisiae*, where septins are necessary for CR formation, fission yeast septins are recruited after the CR has fully assembled (Wu et al., 2003). Septins form first a single ring in late mitosis which splits in two during CR constriction and septum formation. This double ring does not constrict together with the CR, but remains at the base of the septum to delineate the boundaries of the cleavage furrow and dissociates after cell separation (Berlin et al., 2003; Tasto et al., 2003; Wu et al., 2003; An et al., 2004; Juanes and Piatti, 2016; Cortés et al., 2016). Septin mutants have defects in cell-cell separation since septins have a key role, in concert with the exocyst complex, in the delivery of the two septum hydrolytic enzymes (Agn1 and Eng1) to the area around the septum, regulating thereby the step that finishes cytokinesis (Alonso-Nunez et al., 2005; Martin-Cuadrado et al., 2005). Recently, it has also been shown that septins play a role in driving the proper recruitment and maintenance in the septum region of the SIN effector kinase Sid2 and of the glucan synthase enzymes Bgs1 and Ags1, to guarantee a successful cytokinesis (Zheng et al., 2018). Mid2 localizes at the division site after septin recruitment in a septin-dependent manner (Berlin et al., 2003; Ramos et al., 2019). FRAP analysis has revealed that, in the absence of Mid2, septins are more dynamic, indicating a role of Mid2 in septin organization (Berlin et al., 2003). Overexpression of a non-degradable Mid2 mutant let septin filaments persist through the next cell cycle, indicating that Mid2 is also involved in septin ring maintenance (Tasto et al., 2003; An et al., 2004).

How septins and Mid2 are precisely regulated in space and time to properly perform their function and how Mid2 contributes to septin ring organization remains elusive. Here, by using live cell imaging and precise timers for mitotic progression we describe in detail septin and Mid2 behavior in fission yeast. Our approach identified a new step in septin ring assembly: septin filament compaction from a loose meshwork surrounding

the CR into a tight ring when CR constriction is initiated. We show that this step requires Mid2, which has the properties of a bundler for septin filaments promoting their compaction. Polarization microscopy in living dividing cells show that septin filaments transition from a disorganized state to a highly ordered state where they become parallel to the CR actin filaments during CR constriction, in a mechanism dependent on Mid2. Finally, we show that the process of septin compaction requires the SIN pathway signaling and CR constriction. In summary, we show that septin filaments organization depends on the anillin-like protein Mid2 and on signaling inputs that coordinate cytokinesis events in fission yeast.

RESULTS

Septins form a diffuse network in the vicinity of the CR before compacting into a ring structure

Fission yeast septins localize to the division site where they form non-contractile rings defining the edge of the cleavage furrow while the CR constricts and the septum is built (Berlin et al., 2003; Tasto et al., 2003). However, relatively little is known about how septin rings assemble. We therefore decided to characterize by time-lapse imaging the dynamic organization of septins with respect to spindle assembly and elongation, used as a proxy for mitosis progression, and CR assembly and constriction.

To do so, we created a strain producing the septin Spn1 C-terminally fused to GFP, as well as the regulatory light chain of myosin II Rlc1 fused to mCherry to monitor the CR, and the spindle pole body (SPB) component Sid4 tagged with mCherry to monitor the mitotic spindle. Indeed, since septins function strictly as heteromeric complexes, imaging Spn1 is sufficient to have an overview of the whole septin network (An et al., 2004). In these movies, SPB separation was defined as the time for mitotic entry (t=0 in Fig 1).

Septins appeared on the cortex as a band surrounding the CR about 18 minutes after SPB separation, when the SPBs were the furthest apart, corresponding to maximum spindle elongation in anaphase (Fig 1A and 1D, t=18.6 ± 2.3 min). 7 minutes later, septins compacted into a tight ring structure (t=25.6 ± 2.8 min), concomitant with the initiation of CR constriction (t=26.1 ± 2.9 min). This compaction phenomenon is best visualized on

enlargements of the medial region of the cell recorded at 1-minute intervals (Fig 1C left, dark green asterisk). About 20 minutes later, by the end of CR constriction (t=48.5 ± 3.6 min), septins were visualized as a double ring (t=43.4 ± 6.5 min, red asterisk). Eventually, septins re-spread to the new cell tip generated when the two sister-cells separated from one-another by cleavage of the septum (yellow asterisk).

Quantitative analysis of the septin signal further revealed that septin intensity increased for a period of about 15 minutes after they appeared on the medial cortex. The intensity then stayed roughly constant for 30 minutes before decreasing rapidly over 10 minutes (Fig 1E). Furthermore, analyzing the width of the cortical region on which septins were distributed revealed a two-fold reduction in width, from 1.4 ± 0.1 µm at their appearance to 0.75 ± 0.1 µm after compaction when CR constriction starts (n=30, Fig 1F light green dots).

To conclude, this detailed live analysis of septins establishes the timing of the major transitions in septin organization and reveals a new step in the process of septin ring assembly that we have named compaction.

The anillin Mid2 is necessary for septin ring compaction

A similar imaging strategy was taken to define the dynamic organization of the anillin-like protein Mid2, known to co-localize with septins and modulate their dynamics (Berlin et al., 2003; Tasto et al., 2003). Using a strain expressing Mid2 C-terminally fused to the green fluorescent protein ENVY, as well as Rlc1-Cherry and Sid4-mCherry, we found that Mid2 appeared as a narrow band 8 minutes later than septins (t=26.9 ± 2.5 min), coincident with the time of septin compaction (Fig 1C right, light green asterisk in the Mid2 kymograph and Fig 1C left, dark green asterisk in the Spn1 kymograph, Fig 1D) and CR constriction (t=25.2 ± 2.4 min, Fig 1B-E). The Mid2 domain transformed into two rings concomitantly to the double septin rings (Fig 1C, red asterisk) and spread out on the newly formed cell tips at the end of cytokinesis (Fig 1C right, yellow asterisk).

Quantitative analysis of Mid2 signal confirmed the late recruitment of Mid2 compared to septins and showed that its intensity increased for about 30 minutes, stayed constant for 10 minutes and decreased rapidly, similarly to septins (Fig 1E)

The coincidence between CR constriction, septin compaction and Mid2 recruitment suggested that these events may be coupled. To determine if this was the case, we first

tested whether Mid2 was involved in septin compaction. To do so, we analyzed septin ring assembly in a *mid2*Δ mutant (Berlin et al., 2003), using the same markers for mitosis and cytokinesis progression as before. Time-lapse movies showed that in *mid2*Δ cells, initial septin recruitment occurred normally (Fig 2A-D), but septin intensity stopped increasing prematurely, about 8 minutes after septins appeared, i.e. at the time when Mid2 normally appears (Fig 2F). As a consequence, septin maximum intensity was decreased by 3-fold in *mid2*Δ cells compared to control cells (n=6 for each strain; Fig 2E). Furthermore, septin compaction was completely abolished (Fig 2C and 2F). Instead, septins retained a diffuse distribution around the CR and the septum-associated membrane (Fig 2C and S1A). As a consequence, splitting into two rings did not occur. Finally, whereas the CR constriction took place normally (Fig 2D), cell separation was delayed and the diffuse septin network persisted during the next cell cycle, as reported in a *mid2*Δ mutant (Fig 2A-E; Berlin et al., 2003; Tasto et al., 2003).

Mid2 may function as bundler for septin filaments

The fact that Mid2 is necessary for septin compaction, suggested that Mid2 may function as a bundler for septin filaments promoting their alignment and assembly into a ring structure. To perform this activity, Mid2 should be able not only to interact with septins, but also to dimerize or multimerize in order to bridge together two or more septin filaments.

In line with this hypothesis, Mid2 co-immunoprecipitated with Spn1 (see Fig S1B). To test if Mid2 self-associates, we designed co-immunoprecipitation assays between differentially tagged versions of Mid2 co-expressed in the same cells. These experiments were performed in the presence or in the absence of Spn1, to exclude the detection of differentially tagged molecules of Mid2 bridged by septin filaments. Our experiments show that Mid2-mEGFP co-immunoprecipitates with Mid2-13Myc regardless of the presence or absence of Spn1 (Fig 3A). This interaction was also detected even in the absence of Spn1-5 (Fig S2A).

In order to map the Mid2-Mid2 interaction site, we also performed co-immunoprecipitation assays with a truncated version of Mid2 lacking the PH domain (Mid2 ΔPH) or with the isolated PH domain (see Fig 3C for Mid2 domains organization). Interestingly, Mid2 -mEGFP co-immunoprecipitated with Mid2-ΔPH-13Myc and Mid2 PH

domain also showed the ability to self-interact, even in the absence of Spn1 (Fig 3A and 3B). These interactions were also detected in *spn1-5*Δ cells (Fig S2A and B), indicating that Mid2-Mid2 binding is septin-independent. To strengthen this notion, a 2-hybrid assay using Mid2 PH domain as a prey and as a bait was performed; the result suggests that Mid2 PH domain directly interacts with itself (Fig S2C). Furthermore, recombinant GST-Mid2-PH interacted with MBP-Mid2-PH in an *in vitro* binding assay (Fig 3D) showing that the interaction is direct.

To better define the contribution of Mid2 domains to septin ring compaction, we analyzed the function of Mid2-ΔPH lacking the PH domain. This protein has been previously shown not to localize to the division site and therefore it does not contribute to septin function (Tasto et al., 2003). To overcome this situation, Mid2-ΔPH was fused to the GFP-binding protein (GBP) and expressed as a Mid2 unique copy in a strain expressing Spn1-GFP to target it to septins by interaction between the GBP and GFP tags. The analysis of Spn1-GFP indicated that it appeared as a broad band that eventually compacted, in spite of the absence of Mid2 PH domain (Fig 3E and 3F). However, the septin rings collapsed as the CR constricts, suggesting that the PH domain contributes to septin ring stability. It should be noted though that, in this situation, Spn1-GFP tends to form clumps that follow the CR during its constriction and remain longer at the division site. Nonetheless, expression of Spn1-GFP in the *mid2-ΔPH-GBP* background partially rescued the cell separation defect showed by cells lacking Mid2 (Fig 3G).

This altogether indicates that Mid2 has the ability to form structures of higher molecular order and that Mid2 lacking the PH domain domain is sufficient to drive septin compaction, if it is artificially bound to septins. Mid2 PH domain on the other hand may contribute to Mid2 association with septins and to septin ring stability at later stages. Since Mid2 arrival at the cortex also coincides with septin compaction and Mid2 is necessary for this step, our biochemical data support the hypothesis that Mid2 may promote septin compaction by bundling septin filaments.

Septins and Mid2 form wide bands surrounding the CR when cells are blocked in mitosis

Our work shows that septin filaments appear at a very precise time in mitosis, when the anaphase spindle length is maximum, and compact into rings when Mid2 appears and

the CR starts constricting. This provides evidence for a tight coupling between septin ring assembly and cell cycle progression. To get insight into how this coupling is achieved, we first analyzed the localization of Spn1 and Mid2 in mutants blocked in mitosis, with a high cyclin-dependent kinase (CDK) activity. We first used the cold sensitive β-tubulin mutant *nda3-KM311* producing Spn1-GFP or Mid2-ENVY together with Rlc1-mCherry and Sid4-mCherry. Upon cold treatment, cells were blocked in mitosis carrying a CR, and formed a large band of septins and Mid2 surrounding the CR instead of the septin or Mid2 ring detected in control cells (Fig 4A left). Interestingly, Spn1-GFP and Rlc1-mCherry intensity measurements by linescans along the cell axis showed a decrease in Spn1-GFP signal at the exact position of the CR (Fig 4A right and Fig S3A and B). Furthermore, imaging these cells at 1-hour intervals after the temperature shift showed that the septin domain gradually spread along the cortex in *nda3-KM311* cells (from 1.2 µm ± 0.03 after 1 hour at 18°C to 2.4 µm ± 0.2 after 7 hours at 18°C), while narrow rings were always present in control cells (0.9 µm ± 0.03, Fig S3C). A similar situation was observed for the Mid2 domain, its width increasing from 1.0 µm ± 0.1 after 1 hour at 18°C to 2.0 µm ± 0.1 after 7 hours in *nda3-KM311* cells compared to narrow rings in control cells (0.9 µm ± 0.4, Fig S3C). Release from the mitotic block by transferring the cells back to 25°C for 1 hour resulted in a compaction of both septin and Mid2 domains with the domain widths decreasing to 1.2 µm ± 0.1 and 1.3 µm ± 0.2, respectively (Fig S3C).

We also used the thermo-sensitive kinesin-5 *cut7-24* mutant, which forms a monopolar mitotic spindle at 36°C, producing a temporary cell cycle arrest in metaphase with a high CDK activity (Fu et al., 2009; Hagan and Yanagida, 1990; Hagan and Yanagida, 1992). Live cell imaging of the Spn1-GFP Rlc1-mCherry Sid4-mCherry strain in the wild type cells at 36°C slightly accelerated mitosis progression compared to 25°C (Fig 4B and C compared to Fig 1A and D), but septin appearance occurred again at the time of maximum spindle elongation and septin compaction coincided with the initiation of CR constriction, like at 25°C. In the *cut7-24* mutant, since no SPB separation could be observed, the time of transfer to 36°C was defined as time 0 for this experiment. The timing measured in this background can therefore not be compared to those measured in the wild type background. In the *cut7-24* mutant, septins appeared 9 minutes after the temperature

shift in a large band (1.7 ± 0.2 µm compared to 1.45 ± 0.1 µm in control cells, Fig 4F) and were excluded from the CR as seen in *nda3-KM311* cells. Unlike in control cells, where septins compacted to 0.9 ± 0.05 µm, these bands spread along the membrane over time in *cut7-24* cells (2.0 ± 0.1 µm Fig 4D-F), until they escaped the cell cycle arrest 29.6 ± 4.4 min in mean after transfer to 36°C, as visualized by the initiation of CR constriction, which was again coincident with septin band compaction (t=29.3 ± 4.4 min). Later on, septins were observed as two rings at t=41.9 ± 7.3 min until cell separation at t=55.6 ± 5.1 min (Fig 4D and E).

Live cell imaging of the Mid2-ENVY Rlc1-mCherry Sid4-mCherry *cut7-24* mutant strain at 36°C showed that Mid2-ENVY formed a faint band surrounding the CR that enlarged slightly over time (Fig S3D-H), until cells escaped mitosis and CR constriction initiated (t=33.6 ± 2.3 min, Fig S3F-H). Ring splitting and re-spreading were strongly delayed (t=45.7 ± 1.2 min and t=66.4 ± 5.2 min, respectively; Fig S3G).

Overall, these data suggest that high CDK activity does not interfere with initial septin and Mid2 recruitment. However, later events, such as further septin accumulation at the division site and septin compaction and re-spreading may require a reduction in CDK activity. This in turn suggests that Mid2 bundling activity may be impaired upon high CDK activity.

This prompted us to investigate if Mid2 had still the ability to self-interact in this context. To do so, we performed co-immunoprecipitations between Mid2-13Myc and Mid2-GFP, Mid2 ΔPH-GFP or the single PH domain of Mid2 tagged with GFP in the control or *nda3-KM311* mutant cells, after 8 hours of incubation at 18°C to block cells into mitosis (Fig S2D). These experiments did not reveal any modification in the ability of Mid2 to self-interact.

We then tested if high CDK activity could reduce the avidity of Mid2 for septins. To test this hypothesis, co-immunoprecipitation assays between Spn1-GFP and Mid2-13Myc were performed in control and *nda3-KM311* cells after 8 hours of incubation at 18°C or after 8 hours at 18°C followed by 1 hour at 25°C to release cells from the mitotic block (Fig S1B). Although the amount of Mid2 in mitotic cells is higher because its expression

peaks at this stage of the cell cycle (Alonso-Nuñez et al., 2005), these experiments did not reveal significant differences in the ability of Mid2 to interact with septins.

Altogether, these data suggest that, although Mid2 is necessary for septin compaction, it is not proficient for this function when CDK activity is high, independently of its ability to self-interact or to interact with septins. Since Mid2 is hyperphosphorylated during mitosis (Tasto et al., 2003), one hypothesis is that Mid2 phosphorylation prevents septin compaction. Or else, CDK activity regulates septin compaction independently of Mid2.

Mid2 controls the orientation of septin filaments

In order to test further our hypothesis that Mid2 functions as a septin filament bundler and to get insights into the role of Mid2 in septin filament organization, we decided to measure septin filament organization using polarization-resolved fluorescence microscopy (Vrabioiu and Mitchison, 2006; DeMay et al., 2011b; DeMay et al., 2011a; Kress et al., 2013; Wang et al., 2013). Polarimetry measurements with the regular Spn1-GFP fusion, which includes a flexible linker between the septin and the GFP (RIPGLI), revealed randomly oriented GFP dipoles at all stages of cytokinesis (septin recruitment, compaction, splitting and re-spreading) consistent with the flexibly-linked GFP exploring orientations in all directions relative to Spn1 orientation (Fig S4A).

Thus, to use dipole orientation measurements of the GFP as a readout of septin filament orientation, the mobility of GFP relative to Spn1 had to be minimized. We therefore screened for Spn1-GFP fusions in which several amino acids between the C-terminus of Spn1 and the N-terminus of GFP were deleted without impairing Spn1 localization and function nor GFP fluorescence, and identified a fusion of Spn1 to rotationally constrain GFP (conGFP), Spn1-conGFP (see methods for details).

The Spn1-conGFP construct was produced from the genomic *spn1 locus*, under the control of its own promoter, in a strain containing Rlc1-mCherry Sid4-mCherry. This strain had a wild type phenotype indicating that the fusion was functional. Accordingly, Spn1-conGFP localized and redistributed similarly to Spn1-GFP (Fig S4B and C).

We measured GFP dipole orientation at four different stages during cytokinesis, namely septin recruitment (Appearance), septin compaction (Early), CR constriction (Late), and CR disassembly (Post-constriction) in this strain. We found that GFP dipoles were highly disordered when septins are first recruited to the division site, as evidenced by the random distribution of angles between the GFP dipoles and the axis of the CR (Fig 5A). However, at later stages when septins compact into tight rings and throughout CR constriction, the distribution of angles between GFP dipoles and the CR axis became narrow, with GFP dipoles mostly oriented perpendicular to the CR axis (Fig 5A). Their distribution eventually started becoming broader again after CR disassembly, when the septin rings start to collapse. The narrowing of the GFP dipole orientation distributions upon and throughout CR constriction, which also persists post-constriction, indicates that the associated septin filaments are highly organized during these stages.

To determine the orientation of the GFP dipoles relative to septin filaments and be able to deduce septin filament orientation with respect to the CR axis, we took advantage of a Spn4-conGFP fusion, (Fig S4D and E; see methods for detains), which, in addition to its normal localization to the septin ring (white asterisks in Fig S4D), also assembled into ectopic elongated cytoplasmic bars (arrows in Fig S4D). These ectopic bars most likely represent bundles of tightly packed parallel septin filaments, similar to elongated bar-like septin structures induced in *Ashbya gossypii* upon treatment with the septin filament stabilizing drug forchlorfenuron (DeMay et al., 2011a) and very similar to the ectopic bar-like structures detected in *spn2*Δ cells containing both Spn1 and Spn4 (An et al., 2004). GFP dipoles were perpendicular to these septin bars (Fig S4D) suggesting that the septin filaments are oriented perpendicular to the GFP dipole in the Spn4-conGFP fusion. Importantly, GFP dipoles were also perpendicular to the CR axis during CR constriction and disassembly in these cells (Fig S4E), suggesting that septin filaments run parallel to the CR axis of constriction. Given that Spn4 is in a complex with Spn1 (An et al., 2004) we deduce that the septin filaments in the Spn1-conGFP construct are also oriented perpendicular to the GFP dipoles, and propose that initially randomly organized septin filaments orient parallel to the plane of CR constriction upon compaction and keep this orientation throughout CR constriction, progressively losing their organization after CR constriction as septin rings progressively collapse (Fig 5D).

Septin filament orientation was then analyzed in *mid2*Δ cells. Similar to the wild type, septin filaments appeared in a very disorganized manner in *mid2*Δ cells (Fig 5B). However, as CR constriction took place, GFP dipoles failed to reorient perpendicularly to the CR (Fig 5B). Septin filaments also failed to align in *nda3-KM311* cells where CDK activity is high (Fig 5C).

Overall, this data indicates that Mid2 contributes to the orientation of septin filaments parallel to the CR axis of constriction, supporting the hypothesis that Mid2 functions as a septin bundler (Fig 5D) during the septin compaction phase. Moreover, Mid2 bundling activity is negatively regulated by CDK activity in a direct or indirect manner, preventing septin orientation and compaction in early mitosis.

SIN activity and CR constriction are required for normal septin accumulation and compaction at the division site

Since septin compaction is coincident with the initiation of CR constriction, an event known to be triggered by the SIN pathway (McCollum and Gould, 2001), we next wondered if septins and Mid2 were also under the control of this pathway.

To test this hypothesis, we analyzed the behavior of septins in the temperature sensitive hypo-active SIN mutant *sid2-250* at the non-permissive temperature of 36°C (Balasubramanian et al., 1998; Sparks et al., 1999). Live cell imaging of *sid2-250* cells producng Spn1-GFP Rlc1-mCherry Sid4-mCherry revealed that in the majority of cells septins appeared as a diffuse cortical band at the normal timing compared to control cells (Fig 6A). However, the intensity of the septin signal was diminished by ~ 4.5-fold (Fig 6B) and compaction failed in 75% cells, while a loose compaction was observed in the remaining 25%. Indeed, quantification of the extent of compaction showed that, while in control cells the width of the septin domain decreased from 1.5 ± 0.1 µm to 0.9 ± 0.1 µm between appearance and compaction state, in the majority of *sid2-250* mutant cells, the initial width of the septin domain increased instead from 1.6 ± 0.1 µm to 1.9 ± 0.1 µm in a similar period of time, although it decreased in a minority of cells (from 1.6 ± 0.1 µm to 1 ± 0.1 µm (Fig 6C).

The lack of septin compaction suggested a similar defect in the function of Mid2. Therefore, the behavior of Mid2 was analyzed in *sid2-250* cells producing Mid2-ENVY Rlc1-mCherry Sid4-mCherry (Fig S5A). These cells displayed a strong defect (3.5 fold) in the accumulation of Mid2 (Fig S5B), similar to the one observed in Spn1 accumulation.

Altogether, these data suggest that the SIN pathway is not responsible for the initial recruitment of septins or Mid2, but is required for their accumulation. The defects observed in septin compaction points towards an important role of the SIN in this event.

Since the SIN pathway triggers CR constriction, β(1,3)-glucan synthase Bgs1 localization and septum synthesis initiation (Liu et al., 2000; Jin et al., 2006; Cortes et al., 2018), we next wondered if the SIN acts directly on septin compaction or indirectly by inducing CR constriction.

To test this, we decided to use the β(1,3)-glucan synthase mutant *cps1-191* which halts cytokinesis progression due to the inability to construct a septum, with an assembled CR that cannot constrict. Interestingly, it had been shown that the SIN is active in this mutant and required for the stability of the CR (Liu et al., 2000), which provides the best scenario to answer this question. Spn1-GFP and Mid2-ENVY behavior were analyzed in a *cps1-191* mutant producing Rlc1-mCherry and Sid4-mCherry at restrictive temperature (Fig 6D and S4C). Both proteins showed a very defective accumulation (Fig 6E and S4D), septins did not compact (Fig 6F) and eventually dissociated from the division site, even when the CR remained stable (Fig 6D and Fig S5C).

Altogether, these data strongly suggest that the CR itself is not sufficient to promote septin accumulation, and that the SIN pathway, by inducing CR constriction and/or septum synthesis initiation allows septin filaments accumulation. Following Mid2 recruitment, septin filament further accumulate, compact and align parallel to the axis of CR constriction to assemble the septin rings in a process strictly regulated by CR constriction and septum ingression.

DISCUSSION

The assembly of macromolecular structures is a distinctive feature of cytoskeletal elements. Septins are GTP-binding proteins with the ability to form non-polar filaments, which can assemble into a variety of membrane-associated structures such as filament networks or rings (Ong et al., 2014). A number of factors influence the ability of septins to get assembled into those structures, such as the septin monomers themselves, the lipid bilayer composition, post-translational modifications or regulatory proteins.

Here, we investigated the role of the septin-binding protein, Mid2 in the assembly of supramolecular septin filament structures, using fission yeast as a model system. Mid2 is an anillin ortholog, previously involved in the stability of the septin ring assembled during cytokinesis (Berlin et al., 2003; Tasto et al., 2003). Similar to other anillin orthologs, such as *Saccharomyces cerevisiae* Bud4, Mid2 is only recruited at the end of cytokinesis. In contrast to budding yeast, in which septins are first recruited to the presumptive bud site at the onset of G1 (reviewed in (Juanes and Piatti, 2016)), in fission yeast septins only localize to the cortex during cell division. Indeed, septin recruitment requires the assembly of the CR prior to their localization.

Our data indicate that septins localize to the division site as a diffuse band that compacts into a tight ring by the time of CR constriction. Our detailed analysis of septin recruitment shows that the faint band where septins are recruited becomes very intense as septin filament compaction takes place. This might explain the differences found with Wu and collaborators, who established that septins appeared around 22 minutes after SPB separation (Wu et al., 2003). This compaction phenomenon is a novel step in the behavior of septins, coincident with the appearance of Mid2, suggesting a cause-effect relationship. Accordingly, the lack of Mid2 results in the inability of septins to compact.

How might Mid2 trigger septin band compaction? One possibility is that Mid2 serves as a bridge connecting septin filaments. In fact, anillin is a scaffolding protein, able to interact with many other proteins (Field et al., 2005; Piekny and Glotzer, 2008). Anillin (and Mid2) contains a C-terminal septin-interacting domain. If Mid2 were to bundle septin filaments, it should be able to interact with itself so that each molecule could bind to a different septin filament. Our biochemical analysis of Mid2 self-association shows that Mid2 can directly interact with other Mid2 molecules via its C-terminal PH domain. The Mid2 fragment lacking the PH domain can also self-associate independently of

septins (although we cannot rule out that other proteins may bridge this interaction) and is sufficient to trigger septin compaction if an interaction with septins is artificially triggered using the GBP system. This suggests that at least two molecules of Mid2 could bridge two septin filaments together. Increasing levels of Mid2 would contribute to septin filaments compaction into a tight ring. Importantly, in the absence of Mid2, septin accumulation is strongly affected; since Mid2 recruitment to the division site is strongly dependent on septins (Berlin et al., 2003; Tasto et al., 2003), we propose that septins and Mid2 establish a positive feedback loop to get properly accumulated at the division site.

Septin filaments show a dynamic organization pattern during cell cycle progression. Our data based on polarization microscopy let us conclude that septin filaments are not organized when they first appear at initial stages of cytokinesis. Coincident with the arrival of Mid2, septin filaments become aligned parallel to the CR axis of constriction, a pattern that is absent upon deletion of *mid2*. This strongly supports the notion that Mid2 functions to bridge septin filaments and organize them. In budding yeast, after the initial recruitment to the bud site and the early stages of ring formation septins show a "fluid" state, followed by "frozen" state once the ring transforms into a collar (Caviston et al., 2003; Dobbelaere et al., 2003); after ring duplication septin dynamics increases again. At the same time, during the collar stage, septin filaments are parallel to the mother-bud axis (Vrabioiu and Mitchison, 2006), while they reorganize to become parallel to the plane of CR constriction in later stages (DeMay et al., 2011a) in a process that might implicate disassembly and reassembly of septin filaments (Ong et al., 2014). This process might be different in fission yeast, where septin filaments only transition from a disordered to an ordered organization, parallel to the plane of CR constriction. In any case, anillin-like proteins, seem to play the conserved role of septin filament reorganization and septin ring stabilization, as it is also the case for budding yeast anillin Bud4 (McQuilken et al., 2017).

What signals trigger the dynamic behavior of septins? SUMOylation, acetylation and phosphorylation are the best characterized post-translational modifications involved in septin regulation. Our data is consistent with a tight control from the cell cycle machinery. In wild type cells, septin recruitment to the division site takes place during

anaphase, when mitotic spindle reaches its maximum length. Mid2 appearance happens 8 minutes later, by the time of detectable CR constriction and septum synthesis initiation. Analysis of Spn1 and Mid2 behavior in the beta-tubulin mutant *nda3-KM311* or the kinesin-5 mutant *cut7-24*, blocked at early stages of mitosis demonstrate that both, septins and Mid2, strongly accumulate at the division site when CDK activity is high. Although we have no proof of a direct phosphorylation by CDK, Mid2 is highly phosphorylated during septation (Tasto et al., 2003) and our non-published data show a number of CDK consensus sites phosphorylated in *nda3-KM311*-blocked cells. This would not be surprising since both septins and anillin orthologs have been shown to be direct targets of CDK in other model systems (Sinha et al., 2007; Eluere et al., 2012).

Detailed observation of septins and Mid2 in mitotic blocked cells opens two questions. First, septin and Mid2 initial meshworks are physically excluded from the precise CR position on the cortex, raising the question on the molecular mechanisms at work to allow such an exclusion and whether steric hindrance on the plasma membrane surface might be sufficient. Whatever the mechanisms, it can be inferred from this observation that the compaction of the two septin domains on each side of the CR, might immediately produce a double septin ring, although it may not be detectable until the septum has grown enough to push them apart during the maturation stage of the complete septum (Muñoz et al., 2013), allowing the observation of the septin double ring. Initial septin recruitment observation by super-resolution microscopy will contribute to clarify this point.

Second, even though septins and Mid2 co-localize and interact in this context, this is not sufficient to trigger septin ring compaction. This suggests that another mechanism contributes to septin ring compaction. It might involve post-translational modifications of Mid2, additional proteins working together with Mid2 to promote septin filament bundling or yet another mechanism to be identified.

Importantly, compaction of the septin filaments is coincident with the onset of the CR constriction triggered by the SIN pathway and we found the SIN plays a critical role in septin ring assembly. Non-exclusive possibilities may explain this observation. First, it has been shown that septin accumulation is inhibited in latrunculin A-treated cells, in which CR assembly is abolished (Tasto et al., 2003); indeed, although the CR is assembled

is SIN mutants, this ring is not homogeneous and eventually disassembles (Hachet et al., 2008). Second, the poor accumulation of Mid2 in the absence of SIN activity, may arise from the poor accumulation of septin filaments and could also affect their reorganization. This suggests that the SIN, directly or indirectly, regulates Mid2 to control septin accumulation and compaction.

However, we also found that the β(1,3)-glucan synthase Bgs1 mutant allele *cps1-191*, in which the CR assembles and is stable and the SIN pathway is active but CR constriction and initial septum synthesis are defective (Liu et al., 2000), phenocopies the SIN mutant *sid2-250* in terms of septin defects. This suggests a role for the septum structure to trigger septin and Mid2 accumulation and compaction. Although we cannot rule out the hypothesis that the SIN may target Mid2, this demonstrates that SIN activity on its own is not directly responsible for triggering the full accumulation of septins and Mid2 and the compaction of septin filaments. Rather, CR constriction and septum formation by themselves might cooperate with Mid2 to promote septin filament accumulation and reorientation. Indeed, Bgs1 is the only glucan synthase localized to the division site at the time of CR constriction onset (Cortes et al., 2018). One possibility to explore in the future is that CR constriction or the initial deposition of septum material by the β(1,3)-glucan synthase Bgs1 may modify the plasma membrane locally at the ingression furrow, favoring Mid2 and septin accumulation on the cortex and septin filament reorientation.

In summary, we have shown that the crosslinking activity of the anillin-like protein Mid2 promotes the compaction of an initial broad band of septin filaments into tight rings at the onset of CR constriction and septum formation. The activity of the SIN is necessary but not sufficient to trigger this effect and CR constriction and septation themselves, or the β(1,3)-glucan synthase Bgs1 downstream of the SIN may be the real trigger. It will be interesting to explore whether the cleavage furrow acts on the properties of other anillin-like proteins in a similar manner in other systems.

ACKNOWLEDGEMENTS

We thank Vincent Fraisier for maintenance of the microscopes for imaging performed on the Institut Curie, Paris (PICT-IBISA, part of France-Bioimaging national research

infrastructure), Carmen Castro for maintenance of the microscopes performed on IBFG (University of Salamanca/CSIC, Salamanca, Spain) and Cristel Chandre (I2M, CNRS, Marseille, France) for the Polarimetry Analysis application and Matlab codes used for polarimetry data analysis. We are grateful to Henar Valdivieso and Jurg Bähler for strains and plasmids sharing. We also wish to thank to Pilar Pérez and Carlos Rodríguez for their very helpful comments on the manuscript. This work was supported by a grant from Fondation ARC to A.P. Federica Arbizzani received a fourth year PhD fellowship from Fondation ARC. AP is a member of the LabEx CelTisPhyBio. S.A.R. is a Ramon y Cajal fellow from the University of Salamanca (RYC-2016-20652). This work is supported by the Agence Nationale de la Recherche, Fondation ARC pour la Recherche sur le Cancer, the grants PGC2018-094090-B-I00 and PGC2018-098924-B-I00 (Ministerio de Ciencia e Innovación, MICINN, Spain, and ERDF, EU), and CSI150P20 and "Escalera de Excelencia" CLU-2017-03 (Junta de Castilla y León 14-20, Spain and ERDF, EU) and the Agence Nationale pour la Recherche (ANR grant ANR-17-CE13-0014; SEPTIMORF).

AUTHOR CONTRIBUTIONS

Federica Arbizzani performed the experiments, analyzed the data and wrote the manuscript. Manos Mavrakis and Sophie Brasselet performed the polarization microscopy experiments and edited the manuscript. Marta Hoya performed the Mid2 self-interaction experiments. Juan Carlos Ribas checked the functionality of the Mid2-ΔPH-GBP fusion and edited the manuscript. Anne Paoletti and Sergio Rincon directed the study and edited the manuscript.

AUTHOR CONTRIBUTIONS

The authors declare no competing financial interests.

FIGURE LEGENDS

Figure 1: Dynamics of septins and Mid2 during cell division

Time lapse imaging of wild type cells producing Spn1-GFP, Rlc1-mCherry and Sid4-mCherry (**A**) or Mid2-ENVY, Rlc1-mCherry and Sid4-mCherry (**B**) growing at 25°C. Maximum intensity projections of confocal images are shown. Time 0 corresponds to mitotic entry. Scale bars: 4 µm. **C:** Kymographs showing the medial region of the cell producing Spn1-GFP Rlc1-mCherry (left) or Mid2-ENVY Rlc1-mCherry (right). There is a 1-minute interval between successive images. The major transitions in the behavior of Spn1 and Mid2 are indicated with the elapsed time shown in minutes and highlighted at the far right, in magnified panels with an asterisk (color code matches that of the graph in D; green for Spn1 and Mid2 appearance, dark green for Spn1 compaction, magenta for Spn1 and Mid2 splitting and yellow for Spn1 and Mid2 re-spreading). A scheme of a cell and the selected area are shown at the bottom. Scale bars: 2 µm. **D:** Plot depicting the timing of Spn1-GFP (solid bars) and Mid2-ENVY (striped bars) transitions throughout cell division. The indicated times correspond to the elapsed time of each transition, using SPB separation as a timer for mitotic entry (t=0 in A). Mean ± sd are shown. n=51 cells for each strain. **E:** Analysis of Spn1-GFP (light green) and Mid2-ENVY (dark green) fluorescence intensities in the cell middle from mitotic onset throughout cell division. The average line graphics ± sd are displayed. n=6 cells in each case. **F:** Quantification of the extent of Spn1-GFP (light green) width compaction over time. n=30 cells

Figure 2: Defects in septin behavior in the absence of Mid2

Time lapse imaging of wild type (**A**) and *mid2*Δ cells (**B**) producing Spn1-GFP, Rlc1-mCherry and Sid4-mCherry growing at 25°C. Maximum intensity projections of confocal images are shown. Time 0 corresponds to mitotic entry. Scale bars: 2 µm. **C:** Kymographs showing the medial region of wild type (left) or *mid2*Δ cells (right) producing Spn1-GFP, Rlc1-mCherry and Sid4-mCherry, as displayed in the scheme of a cell at the bottom. Frames are spaced by 1-minute intervals. The major transitions in Spn1-GFP dynamics and the defects observed in absence of *mid2* are indicated with the elapsed time shown in minutes and highlighted at the far right, in magnified panels with an asterisk (color code matches that of the graph in D). A scheme of a cell and the selected area are shown at the bottom. Scale bars: 2 µm. **D:** Plot displaying the dynamics of Spn1-GFP in wild type (solid bars) and *mid2*Δ cells (striped bars) throughout cell division. Mean ± sd are shown.

n=52 cells for each strain. **E:** Analysis of Spn1-GFP fluorescence intensity in the cell middle in wild type (green) and in *mid2*Δ cells (magenta) from mitotic onset throughout cell division. The average line graphics ± sd are displayed. n=6 cells in each case. **F:** Quantification of the extent of Spn1-GFP width compaction over time in wild type (green) and in *mid2*Δ cells (magenta). n=20 cells.

Figure 3: Mid2 interacts with other Mid2 molecules through different regions of the protein, contributing to septin compaction

A: Co-immunoprecipitation assay between full length Mid2-mEGFP and Mid2-13Myc or Mid2 ΔPH-13Myc either in the presence (*spn1*$^{+}$) or in the absence of Spn1 (*spn1Δ*). Magenta arrowheads show the expected Mid2 bands; black arrowheads show degradation products; green arrowheads show the immunoglobulin bands. **B:** Co-immunoprecipitation assay between the PH domain of Mid2 tagged with 13XMyc and the PH domain of Mid2 tagged with GFP either in the presence (*spn1*$^{+}$) or in the absence of Spn1 (*spn1Δ*). Magenta arrowheads show the expected Mid2 bands; black arrowheads show degradation products; green arrowheads show the immunoglobulin bands. **C:** Diagram showing the structure of the anillin-like protein Mid2 with the main domains highlighted. **D:** *In vitro* binding assay of recombinant MBP-Mid2-PH with GST-Mid2-PH or GST alone. Left panels show the inputs. Right panels show the GST pulldowns. **E:** Kymographs showing the medial region of wild type (left) or *mid2*Δ*PH-GBP* cells (right) producing Spn1-GFP, Rlc1-mCherry and Sid4-mCherry. There is a 2-minutes interval between successive images. Scale bar: 2 µm. **F:** Quantification of the extent of Spn1-GFP width compaction over time in wild type (green) and in *mid2ΔPH-GBP* cells (magenta). n=20 for wt cells and 25 for *mid2*Δ*PH-GBP* cells. G: Percentage of septating cells in the indicated strains at log phase analyzed by calcofluor staining. Values correspond to the average of 3 experiments, with over 500 cells analyzed per strain each time.

Figure 4: Septins accumulate as a broad band at the cell middle cortex under high CDK activity

A: Epifluorescence images of cells producing Spn1-GFP Rlc1-mCherry Sid4-mCherry (left panels) or Mid2-ENVY Rlc1-mCherry Sid4-mCherry (right panels) in wild type or *nda3-KM311* cells growing at 18°C during 4 hours. Fluorescence intensity analysis of Spn1-GFP, Rlc1-mCherry and Sid4-mCherry signals along the entire cell length of *nda3-KM311* cells incubated during 7 hours at 18°C. Individual lines are shown in light green (wild type cells) and magenta (*nda3-KM311* cells), while average lines are shown in dark green (wild type cells) and purple (*nda3-KM311* cells). n=10 cells (far right panel). A scheme of a cell displaying the linescan used for quantification of fluorescence intensity is shown. Time lapse imaging of wild type (**B**) or *cut7-24* cells (**D**) producing Spn1-GFP, Rlc1-mCherry and Sid4-mCherry growing at 36°C. Maximum intensity projections of confocal images are shown. Time 0 corresponds to mitotic entry. Scale bars: 2 µm. Plot showing Spn1-GFP transitions throughout cell division in the wild type (**C**) or the *cut7-24* mutant (**E**). Mean ± sd are shown. n=45 cells in each case. The graph showing the behavior of the *cut7-24* cells was obtained by the analysis of the cytokinetic events of those cells that escaped the cytokinetic arrest (termed "Escape"). The backward analysis of previous cytokinetic events in the same cells is shown in the "Block" portion of the plot. **F:** Quantification of the extent of Spn1-GFP width compaction over time in wild type (green) and *cut7-24* cells (magenta). n=20 cells in each case.

Figure 5: Septin filament organization changes during CR constriction and septum synthesis depends on Mid2

A: Polar-plot histograms of GFP dipole orientations of Spn1-conGFP filaments from wild type cells at different stages of cytokinesis (top panels). The number of analyzed cells per stage is indicated below each polar-plot histogram (typically 120-200 analyzed pixels per cell). Confocal images of Spn1-conGFP from selected wild type cells and an overlaid color-coded stick representation of the measured orientations (angles ρ) per analyzed pixel at each cytokinetic stage (bottom panels). Scale bar: 1 µm. **B**: Polar plots of GFP dipole orientations of Spn1-conGFP filaments from *mid2*Δ cells at different stages of cytokinesis (top panels). The number of analyzed cells per stage is indicated below each polar-plot histogram. Confocal images of Spn1-conGFP from selected *mid2*Δ cells and an overlaid color-coded stick representation of the measured orientations per pixel, as in

A, at each cytokinetic stage (bottom panels). Scale bar: 1 µm. **C:** Polar plot of GFP dipole orientations of Spn1-conGFP filaments from 57 *nda3-KM311* cells incubated 7 hours at 18°C (top panel). Confocal images of Spn1-conGFP from *nda3-KM311* cells and an overlaid color-coded stick representation of the measured orientations per pixel, as in A (bottom panels). Scale bar: 1 µm. **D**) Schematic representation of septin localization related to major CR and septum transitions (top) and detail of septin filament orientation at each stage (bottom). The cartoon on the bottom right depicts the orientation of a septin filament with respect to the orientation of GFP dipoles (double arrowheads), as deduced from Spn4-conGFP fusions (see Fig S3D and E). The GFP barrels orient with their long axes parallel to the septin filament axis, i.e. with the GFP dipoles perpendicular to the septin filament axis. The numbers correspond to the septin subunits Spn1-4 and the dashed lines delimit a putative octameric septin complex within the filament. The septin subunit order is based on An et al (2004) and their homology with budding yeast septins.

Figure 6: Septin recruitment and compaction are defective in the SIN mutant *sid2-250* and the β(1-3)-glucan synthase Bgs1 mutant *cps1-191*

A: Time lapse imaging of wild type (left series) and *sid2-250* cells (right series), producing Spn1-GFP, Rlc1-mCherry and Sid4-mCherry incubated at 36°C. Maximum intensity projections of confocal images are shown. Time 0 corresponds to mitotic entry. Scale bars: 2 µm. **B:** Analysis of Spn1-GFP fluorescence intensity from mitotic onset throughout cell division in control (green) and *sid2-250* cells (magenta). The average line graphics ± sd are displayed. n=6 cells in each case. **C:** Quantification of the extent of Spn1-GFP width compaction over time in wild type (green) and *sid2-250* cells (magenta). Note that some *sid2-250* cells escape SIN phenotype. n=20 cells. **D:** Time lapse imaging of wild type (left series) and *cps1-191* cells (right series), producing Spn1-GFP, Rlc1-mCherry and Sid4-mCherry incubated at 36°C. Maximum intensity projections of confocal images are shown. Time 0 corresponds to mitotic entry. Scale bars: 2 µm. **E:** Analysis of Spn1-GFP fluorescence intensity from mitotic onset throughout cell division in control (green) and *cps1-191* cells (magenta). The average line graphics ± sd are

displayed. n=6 cells. **F:** Quantification of the extent of Spn1-GFP width compaction over time in wild type (green) and *cps1-191* cells (magenta). n=20 cells in each case.

EXPERIMENTAL PROCEDURES

Yeast genetics and culture conditions

Standard *S. pombe* media and genetic manipulations were used as described in (Moreno et al., 1991). All strains used in the study were isogenic to wild type h^- 972 and are described in Supplemental Table S1. Strains from genetic crosses were selected by random spore germination and replica in plates with the appropriate supplements or drugs.

Plasmids and DNA transformations were performed by using the lithium acetate-DTT method. Briefly, 20 ml of exponentially growing cells (optical density 0.5-0.8 at 600 nm) were harvested by centrifugation and washed with 10 mM Tris HCl pH 7.4. Then, these cells were re-suspended in 100 mM lithium acetate with 10 mM DTT and incubated on an orbital wheel at room temperature for 40 minutes. 100 µl of these cells were mixed with 80 µl of 100 mM lithium acetate, 10 µl of single stranded DNA from salmon testes (D9156-5ML, Sigma) and 2 µg of the desired plasmid or the purified PCR product. After 10 minutes of incubation at room temperature on an orbital wheel, 300 µl of PEG 4000, previously diluted 1:1 in 100 mM lithium acetate, were added. After a second round of 10 minutes at room temperature on the wheel, 15 µl of DMSO were added and the cells were subjected to heat shock at 42°C for 20 minutes in a water bath. Cells were then washed, resuspended in 100 µl of sterile water and plated on the appropriate selection plates.

Production of mutant and tagged strains

Wild type *mid2* was fused to the DNA sequence coding for the green fluorescent tag ENVY (Slubowski et al., 2015) or for the 13Xmyc tag at its 3' end by PCR amplification of a cassette with the corresponding fusion from the plasmid pFA6a-*ENVY-kanMX6* or pFA6a-*13Xmyc-natMX6*, respectively, as described in (Bahler et al., 1998).

To create the strains used for the co-immunoprecipitation experiments shown in Figures 3A, S1B and S2D, constructs containing *mid2*$^{+}$, or the *mid2* fragments coding for Mid2-ΔPH (aminoacids 1-581) or for the PH domain of Mid2 (aminoacids 582-685) were cloned into a pJK148-derived plasmid (Keeney and Boeke, 1994) containing *mEGFP* followed by the terminator of *nmt1*$^{+}$, to be expressed under the control of the *mid2*$^{+}$ promoter. The resulting plasmids were digested with NruI or Tth111 for plasmid linearization to allow integration in the endogenous *leu1-32 locus* upon yeast transformation.

To create the strains used for the co-immunoprecipitation experiments shown in Figures S2A and B, an integration plasmid for Mid2 constructs was made by insertion of 1 kb of the *mid2*$^{+}$ promoter and terminator into pFA6a-*mEGFP-kanMX6* (Bahler et al., 1998) between SalI and BamHI sites and PmeI and SacII sites, respectively. The *mid2*$^{+}$ open reading frame was then inserted upstream of *mEGFP* between BamHI and XmaI. The *mid2* fragments coding for Mid2-ΔPH (aminoacids 1-569) or for the PH domain of Mid2 (aminoacids 569-706) were cloned into this plasmid, replacing full length *mid2*$^{+}$, to express the Mid2 truncations used for co-immunoprecipations in figure 1. pFA6a-*GFP-kanMX6*-derived plasmid was digested with NotI to release the linear DNA fragment that directs homologous recombination upon yeast transformation.

For production of Mid2-13Myc truncations in Figures S2A and B, 1 kb of the *mid2*$^{+}$ promoter was cloned into pBP-*ade6* (Beaudoin et al., 2006) using the sites SalI and XmaI. The resulting plasmid was used to clone a fragment coding for *13xmyc* and 1 kb of *nmt1*$^{+}$ terminator obtained from pSR98 (Rincon et al., 2014) using the sites NotI and SacI. Finally, the *mid2* truncations were cloned in this plasmid using the sites XmaI and NotI. The resulting plasmids were digested with AatII for plasmid linearization to allow integration in the endogenous *ade6*$^{+}$ *locus* upon yeast transformation.

To create the strains used for the co-immunoprecipitation experiment shown in Figure 3B, a construct containing the *mid2* fragment coding for the PH domain of Mid2 (aminoacids 582-685) was cloned into a pJK148-derived plasmid containing *13xMyc* followed by the terminator of *nmt1*$^{+}$, to be expressed under the control of the *mid2*$^{+}$ promoter. The resulting plasmids were digested with NruI for plasmid linearization and integration in the endogenous *leu1-32 locus* of a strain containing the PH domain of Mid2 (aminoacids 582-685) followed by *mEGFP* expressed from *mid2*$^{+}$ endogenous *locus*.

DNA constructs expressing Mid2-mEGFP full length, Mid2ΔPH-mEGFP (1-581aa) and the C-terminal PH domain of Mid2 (aa 582-685) tagged with mEGFP, used in figure S2D were integrated at the *leu1-32 locus* under the control of *mid2⁺* promoter. Briefly, a fragment containing 1 kb of *mid2⁺* promoter and the different *mid2* fragments were amplified from genomic DNA purified from a wild type strain and cloned between KpnI and NotI sites of pSR2 (pJK148 - *Pcdr2⁺-cdr2⁺-GFP-Tnmt1⁺*) (Keeney and Boeke, 1994). The plasmids obtained were circularized by NruI or Tth111 digestion to allow integration into the *leu1-32* locus of a wild type strain.

A DNA construct expressing the PH domain of Mid2 (582-685 aa) was integrated into the *leu1-32* locus under the control of *mid2⁺* promoter. Briefly, a fragment containing 1 kb of *mid2⁺* promoter and the *mid2* fragment coding for the PH domain of Mid2 (582-685aa) were amplified from genomic DNA purified from a wild type strain and cloned between KpnI and NotI sites of pSR98 (pJK148 *Pcdr2⁺-cdr2⁺-13xMyc-Tnmt1⁺*) (Rincon et al., 2014). The obtained plasmid was linearized by NruI digestion to allow integration into the *leu1-32* locus of a wild type strain.

To create the strains producing Spn1 fused to monomeric superfolder GFP lacking the 12 N-terminal aminoacids (Spn1-conGFP, *spn1⁺-msfGFPΔN12)*, the msfGFP sequence was first amplified from plasmid pEX-A128-*msfGFP* and cloned into the pFA6a-*EGFP-kanMX6* plasmid (Bahler et al., 1998), replacing the original EGFP for msfGFP using the Gibson Assembly cloning strategy (Gibson et al., 2009). *msfGFPΔN12* and *spn1⁺* were amplified and fused in a two-round PCR and the PCR product was used to replace *msfGFP* in the pFA6a-*msfGFP-kanMX6* plasmid. This construct was amplified with long oligos containing 80 bases from *spn1⁺* promoter and terminator to direct the homologous recombination, producing the integration module which was used to transform the wild type, *mid2*Δ and *nda3-KM-311* strains and replace *spn1⁺* with *spn1⁺-msfGFPΔN12*. A similar strategy was used to create the strains producing Spn4 lacking the 6 C-terminal aminoacids fused to GFP lacking the 7 N-terminal aminoacids (Spn4-conGFP, *spn4-ΔC6-mEGFP-ΔN7)*.

To create the strains producing Mid2-ΔPH-GBP, a DNA fragment coding for the GFP binding protein was obtained from pFA6a-*GBP-kanMX6* (Chen et al., 2017) by digestion with PacI-AscI, and cloned into the plasmid pFA6a-*mid2⁺-mEGFP-kanMX6*, replacing the

mEGFP for GBP. The obtained plasmid was linearized by digestion with NotI before yeast transformation.

All plasmids were confirmed by PCR and restriction enzyme digestion, and the DNA fragments amplified by PCR were confirmed by DNA sequencing.

Microscopy and image analysis

Cells were incubated at 25°C in YE5S except in the case of cell cycle temperature sensitive mutants (*cut7-24, sid2-250, cps1-191*), which were incubated for 3 hours at 36°C or *nda3-KM311* cold sensitive mutant, which was incubated up to 7h at 18°C.

Epifluorescence images were taken on a DMRXA2 upright microscope (Leica Microsystems), equipped with a 100×/1.4NA oil immersion PlanApo objective and a Coolsnap HQ CCD camera (Photometrics). The exposure time was 2 s for GFP, 1 s for mCherry. Quantification in the *nda3-KM311* mutant of Spn1-GFP fluorescence intensity with respect to the red fluorescence signal was performed by analysis along a line drawn throughout the cell length (dashed lines in Fig 4A and Fig S3A and B). The values obtained were background-substracted using an equivalent region outside the cell. The line graphics obtained were then centered with respect to the position of the ring.

For time-lapse imaging, 1 ml of exponentially growing cells were harvested by centrifugation for 60 s at 800 g in a Minispin Eppendorf centrifuge equipped with a F-45-12-11 rotor, most of the supernatant was discarded and 1 µl of the cells was deposited in a 2% YE5S agar pad at the center of polydimethylsiloxane slide chamber prepared as described in (Costa et al., 2013).

Time-lapse movies were performed on an inverted spinning disk confocal microscope (Roper/Nikon Instruments), equipped with a Plan Apochromat 100×/1.4 NA objective (Nikon Instruments), a PIFOC (perfect image focus) objective stepper, and a charge-coupled device camera (EMCCD 512x512 QuantEM; Photometrics). The microscope was equipped with a thermostatic methacrylate chamber to perform imaging at 25°C (or 36°C when analyzing thermosensitive mutants). To analyze Spn1-GFP Rlc1-mCherry Sid4-mCherry wild type as well as Mid2-ENVY Rlc1-mCherry Sid4-mCherry in the respective cell cycle thermosensitive mutants, z-stacks of 7 planes spaced by 1 µm between planes were acquired at 1 min interval for 3h (binning 1, 300 EM gain; 200 ms exposure for each channel).

Fluorescent images for each channel were scaled equivalently to their respective control and analyzed with MetaMorph software 7.7.8.

Analysis of Spn1-GFP and Mid2-ENVY fluorescent signals were quantified in cells at mitotic onset (SPBs separation) by measuring the average fluorescence intensity of the medial region with the linescan tool (Metamorph software 7.7.8) of 5 µm in length and 13 µm in width perpendicularly oriented to the long axis of the cell on maximum intensity projection images. Background values, measured as the average intensity of an equivalent region outside the cell, were then subtracted.

To compare the width of Spn1-GFP and Mid2-ENVY at the two different time points indicated in the text in control and mutant cells, the linescan tool (MetaMorph software 7.7.8) was oriented parallel to the long axis of the cell. The values obtained are the average of 3 measurements over the cell width within the bands corresponding to Spn1-GFP or Mid2-ENVY.

Co-immunoprecipitation experiments

Co-immunoprecipation experiments were performed as described in (Guzman-Vendrell et al., 2013). For the experiments shown in figures 3A and B and S1B and S2D, 200 ml of early log phase cells were incubated to an optical density of 1.0 at 600 nm at 25°C in YE5S medium concentrated twice compared to the regular YE5S medium (YE5S2X), harvested in cold STOP buffer (150 mM NaCl, 50 mM NaF, 10 mM EDTA, 1 mM NaN3) and resuspended in 300 µl Lysis buffer (50 mM Hepes, 100 mM NaCl, 1 mM EDTA, 1 % NP-40, 50 mM NaF, 20 mM β-glycerophosphate) with 1 mM PMSF and a tablette of protease inhibitor cocktail (Thermo, 11697498001). Extracts were incubated with anti-mouse IgG magnetic beads (M-280 DYNAL, Invitrogen), previously coupled to 6 µg of anti-GFP mAb (Roche). For the experiments shown in figure S2A and B, 200 ml of early log phase cells were incubated to an optical density of 0.7 at 600 nm at 25°C in YE5S medium harvested in cold STOP buffer, and finally resuspended in 300 µl Lysis buffer with proteases inhibitors (1 mM PMSF, 0.5 µM aprotinin, 0.5 µM leupeptin, 0.5 µM pepstatin A, 0.1 µM NaVO3). Extracts were incubated with protein A-magnetic beads (Thermo, 10006D) previously conjugated with 5 µl of polyclonal anti-GFP antibody (Thermo A-6455).

Western blots were probed with mouse anti-GFP mAb (1/500 dilution, Roche Cat No. 11814460001) or mouse anti-myc mAb 9E10 (1/666 dilution, Roche Cat No. 11667149001). Secondary goat anti-mouse antibodies were coupled to horse radish peroxidase (Jackson Immunoresearch).

For *nda3-KM311* synchronization experiments, 1 liter of cell culture was incubated overnight to an optical density of 0.6 at 600 nm. Then, the cells were synchronized by an 8 hours incubation at 18°C before being collected and processed.

***In vitro* binding assay**

DNA fragments encoding Mid2 PH domain (aminoacids 569-706) were PCR-amplified and inserted into the GST-producing vector pJC20 or the MBP-producing vector pMAL-p2 (New England Biolabs Inc.) between the sites NdeI - BamHI or BamHI – SalI, respectively. The resulting plasmids were transformed into the E. coli strain BL21. 200 ml of LB cultures supplemented with ampicillin at an O.D. of 2.0 at 600 nm after induction of protein production with 0.1 mM IPTG for 3 h at 28 °C were harvested. For GST fusions, cells were resuspended and incubated 30 min at room temperature in 10 ml of CelLytic B Cell Lysis Reagent (Sigma-Aldrich, C8740) containing 50 u/ml Benzonase (Sigma-Aldrich, E1014), 1 mg/ml lysozyme and protease inhibitors (1 mM PMSF, 0.5 µM aprotinin, 0.5 µM leupeptin, 0.5 µM pepstatin A). After a centrifugation at 10.000 x g for 30 min at 4 °C, the lysate was incubated with 100 µl glutathione-conjugated magnetic beads (Cube Biotech) in rotation overnight at 4 °C. The beads were then PBS-washed three times and resuspended in 200 µl of binding buffer (20 mM Tris-HCl pH 7.5, 0.2 M NaCl, 1 mM EDTA, 0.5 % NP-40). For MBP fusions, cells were resuspended and incubated 10 min in rotation at room temperature in mM Tris-HCl pH 8.0, 20 % sucrose, 1 mM EDTA (80 ml of buffer per gram of cells). After centrifugation, the pellet was incubated for 10 minutes in ice in 80 ml of 5 mM $MgSO_4$buffer per gram of cells, frequently shaking gently. After a centrifugation at 8.000 x g for 20 min at 4 °C, 800 µl of 50 % of amylose resin (NEB, E8021) per 40 ml of lysate and Tris-HCl pH 7.5 to a final concentration of 20 mM were added and incubated in rotation at 4 °C overnight. The resin was then washed three times in washing buffer (20 mM Tris-HCl pH 7.5, 200 mM NaCl, 1 mM EDTA) and the MBP fusions were eluted by adding a total of 6 ml 10 mM maltose. Samples were concentrated using a Y-30 centricon after washing five times with binding buffer. 30 µl

of GST or GST-Mid2-PH were mixed with30 µl MBP-Mid2-PH in a total volume of 100 µl and incubated at 4 °C for 2 h. Magnetic beads were washed three times with binding buffer, resuspended in 35 µl of laemli buffer and analyzed by SDS-PAGE and western blotting.

Septin-GFP fusions for orientation measurements

The Spn1-GFP fusion used throughout this study includes a flexible linker (RIPGLI) between the Spn1 and the GFP sequences rendering this fusion not appropiate for orientation measurements (Fig S3A). To generate fusions of septins with rotationally constrained GFP (conGFP) we generated and screened C-terminal GFP fusions of Spn1 and Spn4 with no linker sequence between the septin and the GFP, and with the C-termini of septins and the N-terminus of GFP truncated to different extents, indicated as δC and ΔN, respectively. The coiled-coil prediction algorithm COILS was used to identify the ends of the predicted coiled-coils in Spn1 and Spn4 to guide the C-terminal truncations. We started with Spn1 fusions to monomeric EGFP (mEGFP) deleting C-terminal Spn1 and N-terminal GFP amino acids, generating Spn1ΔC5-mEGFPΔN5 (Spn1 1-464; mEGFP starting at EELF), Spn1ΔC5-mEGFPΔN6, Spn1ΔC5-mEGFPΔN7 and Spn1ΔC5-mEGFPΔN11; the first three fusions behaved normally localization- and septation-wise, but the GFP was still flexible, whereas the last one was not fluorescent. Further trimming of Spn1 C-terminus to generate Spn1ΔC12-mEGFPΔN5, Spn1ΔC12-mEGFPΔN6 and Spn1ΔC12-mEGFPΔN7 led to ectopic cytoplasmic bar-like structures (like the ones shown in FigS3 D). We thus turned to monomeric superfolder GFP (msfGFP) which tolerates more extensive N-terminal truncations (Pédelacq et al., 2006), and generated a fusion of full-length Spn1 to msfGFP without using a linker and additionally removing residues before the first stave of the GFP β-barrel to obtain Spn1-msfGFP-ΔN12 (Spn1 1-469; msfGFP starting at VPILV). Spn1-msfGFPΔN12, designated as Spn1-conGFP in this study, was rotationally constrained and was used for orientation measurements. We also generated Spn4 fusions to mEGFP deleting C-terminal Spn4 and N-terminal GFP amino acids to obtain Spn4ΔC6-mEGFPΔN5 (Spn4 1-374; EGFP starting at EELF), Spn4ΔC6-mEGFPΔN6, Spn4ΔC6-mEGFPΔN7 and Spn4ΔC6-mEGFPΔN11. The first two constructs behaved normally, the third one formed ectopic cytoplasmic bar-

like structures in addition to its localization in septin rings (Fig S3D), whereas the last one was not fluorescent. The GFP in Spn4ΔC6-mEGFPΔN7 was rotationally constrained and this fusion, designated as Spn4-conGFP in this study, was used to infer the orientation of septins with respect to the GFP dipole.

Spinning-disk polarization-resolved fluorescence microscopy

Yeast cells were prepared for live polarimetry measurements as described above for live microscopy. Polarization-resolved fluorescence images were acquired on a custom-built optical setup employing a confocal spinning disk unit (CSU-X1-M1 from Yokogawa) connected to the side-port of a Perfect Focus System-equipped inverted microscope (Eclipse Ti2-E, Nikon Instruments), using a Nikon Plan Apo ×100/1.45 NA oil immersion objective lens, 488- and 561-nm Sapphire laser lines (Coherent) and an iXon Ultra 888 EMCCD camera (1024×1024 pixels, 13×13 μm pixel size, Andor, Oxford Instruments), resulting in an image size of 1 pixel = 65 nm. Polarimetry images were obtained by varying the incident linear polarization with a Pockels Cell electro-optic modulator (No 28-NP Quantum Technology) synchronized to the EMCCD camera, followed by a quarter waveplate (WPQ05M-488, Thorlabs) (Wang et al., 2013). The quality of the polarization state at the sample plane was ensured by using a compensating dichroic beamsplitter similar to the one present in the spinning disk unit (405/488/561/635 nm Quad Dichroic mirror) but placed at 90° reflection to exchange s and p polarization state phase-shifts. A polarization stack is made of 18 polarized images using an incident linear polarization varying from 0° (correspoding to the horizontal direction in the image) to 170° with steps of 10°. The recorded stack is used to obtain the polarization response of the sample at each pixel, from which GFP orientation information can be deduced. Three to five large field-of-view images (66×66 μm) typically containing 10-20 cells during cytokinesis per image, were collected for wild-type and *nda3-KM311* cells; seven to eight such images were collected for *mid2*Δ cells to account for the smaller number of *mid2*Δ dividing cells per field of view. An exposure time of 0.5 s was used per image. Before each polarimetry measurement, a two-color z-stack was acquired (Δz = 1.0 μm) to image both septin-GFP fusions and myosin/spindle bodies; these images were used for staging the measured cells and correlating the measured orientation distributions with the different stages of cytokinesis. A polarization stack was then recorded for each position within a z-stack (Δz

= 1.0 μm) for the septin-GFP channel, and thus allowed to obtain polarimetry images throughout the septin rings, containing both tangential-most views where the entirety of the ring can be seen parallel to the xy plane, and more equatorial views showing cross-sections that appear as spots on either side of the ring. To minimize bias in the measured orientations due to the contribution of off-plane orientations we focused on the tangential-most views, as shown in Fig 5 and Fig S3.

Polarization stack images were first processed with the open-source image processing software ImageJ/Fiji. Images within each polarization stack were systematically registered using the StackReg plugin to correct for drift during the acquisition. The proper z planes, i.e. the ones containing the tangential-most views of the ring, were then identified for each cell, and polarimetry data were analyzed according to the framework defined by (Kress et al., 2013) to obtain the mean GFP dipole orientation (angle ρ) per pixel. Analysis and data representation, including color-coded stick representations of the measured orientations per pixel and polar-plot histograms, were done by using the Polarimetry Analysis software which is a Matlab App Designer standalone application. The source code is available at gitHub.com/cchandre/Polarimetry, and the desktop app can be freely obtained at https://www.fresnel.fr/polarimetry under a BSD license.

The regions of interest for analysis were selected by a combination of intensity thresholding and manual selection of the features to analyze. Each region of interest contained typically 120-200 analyzed pixels i.e. 120-200 orientation color-coded sticks in the tangential-most view of the septin ring per cell (Fig 5 and Fig S3). The mean orientation per pixel is represented as a stick whose orientation and color are the measured angle ρ within the resolution limit of the microscope (~200 nm). The distribution of mean orientations was represented in 0-180°polar-plot histograms. To assess the extent to which the measured orientations were more parallel or more perpendicular with respect to the CR axis, the ring axis in each cell was used to normalize the angle distributions from 0-180° to 0-90° and generate 0-90° polar plots (Fig 5 and Fig S3), with 0° and 90° defining orientations parallel and perpendicular to the ring axis, respectively. To facilitate the visual comparison of orientation distributions between cells and also relate directly to the 0-90° polar plots, representative cells in Fig 5 and Fig S3 have been rotated using the Polarimetry Analysis software so that their CR axes correspond to the horizontal orientations (0°). 0-90° normalized polar-plot histograms

from all cells in a given condition were concatenated to represent all analyzed data in each condition, then they were rescaled to their respective maximum value to facilitate comparisons, and orientations were sorted in bins of 6°. The normalization of orientation distributions with respect to the CR ring axis, the normalization of 0-180° to 0-90° polar plots and the rescaling of histograms were done with custom-generated Matlab codes, the source codes of which are available at gitHub.com/cchandre/Polarimetry.

Statistical analysis

The number of samples analyzed (n) is defined in each figure and were derived from 3 independent experiments, except for the co-immunoprecipitations assays in Figure S1B and S2D, which were repeated twice. The error bars correspond to standard deviation (sd) between experiments and are specifically indicated in each figure.

SUPPLEMENTAL INFORMATION

Supplemental information includes five figures and one table.

REFERENCES

Alonso-Nunez, M.L., An, H., Martin-Cuadrado, A.B., Mehta, S., Petit, C., Sipiczki, M., del Rey, F., Gould, K.L., and de Aldana, C.R. (2005). Ace2p controls the expression of genes required for cell separation in Schizosaccharomyces pombe. Mol Biol Cell *16*, 2003-2017.

An, H., Morrell, J.L., Jennings, J.L., Link, A.J., and Gould, K.L. (2004). Requirements of fission yeast septins for complex formation, localization, and function. Mol Biol Cell *15*, 5551-5564.

Bahler, J., Wu, J.Q., Longtine, M.S., Shah, N.G., McKenzie, A., 3rd, Steever, A.B., Wach, A., Philippsen, P., and Pringle, J.R. (1998). Heterologous modules for efficient and versatile PCR-based gene targeting in Schizosaccharomyces pombe. Yeast *14*, 943-951.

Balasubramanian, M.K., McCollum, D., Chang, L., Wong, K.C., Naqvi, N.I., He, X., Sazer, S., and Gould, K.L. (1998). Isolation and characterization of new fission yeast cytokinesis mutants. Genetics *149*, 1265-1275.

Beaudoin, J., Laliberté, J., Labbé, S. (2006). Functional disection of tr4 and Ctr5 amino-terminal regions reveals motifs with redundant roles in copper transport. Microbiology (Reading) *152*:209-222.

Berlin, A., Paoletti, A., and Chang, F. (2003). Mid2 stabilizes septin rings during cytokinesis in fission yeast. J Cell Biol *160*, 1083-1092.

Bertin, A., McMurray, M.A., Thai, L., Garcia, G., 3rd, Votin, V., Grob, P., Allyn, T., Thorner, J., and Nogales, E. (2010). Phosphatidylinositol-4,5-bisphosphate promotes budding yeast septin filament assembly and organization. J Mol Biol *404*, 711-731.

Bhavsar-Jog, Y.P., and Bi, E. (2017). Mechanics and regulation of cytokinesis in budding yeast. Semin Cell Dev Biol *66*, 107-118.
Bridges, A.A., and Gladfelter, A.S. (2015). Septin Form and Function at the Cell Cortex. J Biol Chem *290*, 17173-17180.
Bridges, A.A., Jentzsch, M.S., Oakes, P.W., Occhipinti, P., and Gladfelter, A.S. (2016). Micron-scale plasma membrane curvature is recognized by the septin cytoskeleton. J Cell Biol *213*, 23-32.
Bridges, A.A., Zhang, H., Mehta, S.B., Occhipinti, P., Tani, T., and Gladfelter, A.S. (2014). Septin assemblies form by diffusion-driven annealing on membranes. Proc Natl Acad Sci U S A *111*, 2146-2151.
Cauvin, C., and Echard, A. (2015). Phosphoinositides: Lipids with informative heads and mastermind functions in cell division. Biochim Biophys Acta *1851*, 832-843.
Caviston, J.P., Longtine, M., Pringle, J.R., and Bi, E. (2003). The role of Cdc42p GTPase-activating proteins in assembly of the septin ring in yeast. Mol Biol Cell *14*, 4051-4066.
Chen, Y.H., Wang, G.Y., Hao, H.C., Chao, C.J., Wang, Y., and Jin. Q.W. (2017). Facile manipulation of protein localization in fission yeast through GBP-GFP binding. J Cell Sci *130*:1003-1015.
Cortés, J.C.G., Ramos, M., Osumi, M., Pérez, P., and Ribas, J.C. (2016). The Cell Biology of Fission Yeast Septation. Microbiol Mol Biol Rev *80*, 779-791.
Cortés, J.C.G., Ramos, M., Konomi, K., Barragán, I., Moreno, M.B., Alcaide-Gavilán, M., Moreno, S., Osumi, M., Pérez, P., and Ribas, J.C. (2018). Specific detection of fission yeast primary septum reveals septum and cleavage furrow ingression during early anaphase independent of mitosis completion. PLoS Genet *14*, e1007388.
Costa, J., Fu, C., Syrovatkina, V., and Tran, P.T. (2013). Imaging individual spindle microtubule dynamics in fission yeast. Methods Cell Biol *115*, 385-394.
DeMay, B.S., Bai, X., Howard, L., Occhipinti, P., Meseroll, R.A., Spiliotis, E.T., Oldenbourg, R., and Gladfelter, A.S. (2011a). Septin filaments exhibit a dynamic, paired organization that is conserved from yeast to mammals. J Cell Biol *193*, 1065-1081.
DeMay, B.S., Noda, N., Gladfelter, A.S., and Oldenbourg, R. (2011b). Rapid and quantitative imaging of excitation polarized fluorescence reveals ordered septin dynamics in live yeast. Biophys J *101*, 985-994.
Dobbelaere, J., and Barral, Y. (2004). Spatial coordination of cytokinetic events by compartmentalization of the cell cortex. Science *305*, 393-396.
Dobbelaere, J., Gentry, M.S., Hallberg, R.L., and Barral, Y. (2003). Phosphorylation-dependent regulation of septin dynamics during the cell cycle. Dev Cell *4*, 345-357.
Echard, A., Hickson, G.R., Foley, E., and O'Farrell, P.H. (2004). Terminal cytokinesis events uncovered after an RNAi screen. Curr Biol *14*, 1685-1693.
El Amine, N., Kechad, A., Jananji, S., and Hickson, G.R. (2013). Opposing actions of septins and Sticky on Anillin promote the transition from contractile to midbody ring. J Cell Biol *203*, 487-504.
Eluere, R., Varlet, I., Bernadac, A., and Simon, M.N. (2012). Cdk and the anillin homolog Bud4 define a new pathway regulating septin organization in yeast. Cell Cycle *11*, 151-158.
Estey, M.P., Di Ciano-Oliveira, C., Froese, C.D., Bejide, M.T., and Trimble, W.S. (2010). Distinct roles of septins in cytokinesis: SEPT9 mediates midbody abscission. J Cell Biol *191*, 741-749.
Field, C.M., Coughlin, M., Doberstein, S., Marty, T., and Sullivan, W. (2005). Characterization of anillin mutants reveals essential roles in septin localization and plasma membrane integrity. Development *132*, 2849-2860.
Founounou, N., Loyer, N., and Le Borgne, R. (2013). Septins regulate the contractility of the actomyosin ring to enable adherens junction remodeling during cytokinesis of epithelial cells. Dev Cell *24*, 242-255.

Fu, C., Ward, J.J., Loiodice, I., Velve-Casquillas, G., Nedelec, F.J., and Tran, P.T. (2009). Phospho-regulated interaction between kinesin-6 Klp9p and microtubule bundler Ase1p promotes spindle elongation. Dev Cell *17*, 257-267.
Fujiwara, T., Bandi, M., Nitta, M., Ivanova, E.V., Bronson, R.T., and Pellman, D. (2005). Cytokinesis failure generating tetraploids promotes tumorigenesis in p53-null cells. Nature *437*, 1043-1047.
Gibson, D.G., Young, L., Chuang, R-Y., Venter, J.C., Hutshison, C. A., and Smith, H. O. (2009). Enzymatic assembly of DNA molecules up to several hundred kilobases. Nat Methods *6*, 343-5.
Gladfelter, A.S., Pringle, J.R., and Lew, D.J. (2001). The septin cortex at the yeast mother-bud neck. Curr Opin Microbiol *4*, 681-689.
Guzman-Vendrell, M., Baldissard, S., Almonacid, M., Mayeux, A., Paoletti, A., and Moseley, J.B. (2013). Blt1 and Mid1 provide overlapping membrane anchors to position the division plane in fission yeast. Mol Cell Biol *33*, 418-428.
Hachet, O., and Simanis, V. (2008). Mid1p/anillin and the septation initiation network orchestrate contractile ring assembly for cytokinesis. Genes Dev *22*, 3205-16.
Hagan, I., and Yanagida, M. (1990). Novel potential mitotic motor protein encoded by the fission yeast cut7+ gene. Nature *347*, 563-566.
Hagan, I., and Yanagida, M. (1992). Kinesin-related cut7 protein associates with mitotic and meiotic spindles in fission yeast. Nature *356*, 74-76.
Hartwell, L.H. (1971). Genetic control of the cell division cycle in yeast. II. Genes controlling DNA replication and its initiation. J Mol Biol *59*, 183-194.
Hergovich, A., Stegert, M.R., Schmitz, D., and Hemmings, B.A. (2006). NDR kinases regulate essential cell processes from yeast to humans. Nat Rev Mol Cell Biol *7*, 253-264.
Hickson, G.R., and O'Farrell, P.H. (2008). Anillin: a pivotal organizer of the cytokinetic machinery. Biochem Soc Trans *36*, 439-441.
Jin, Q.W., Zhou, M., Bimbo, A., Balasubramanian, M.K., and McCollum, D. (2006). A role for the septation initiation network in septum assembly revealed by genetic analysis of sid2-250 suppressors. Genetics *172*, 2101-2112.
Juanes, M.A., and Piatti, S. (2016). The final cut: cell polarity meets cytokinesis at the bud neck in S. cerevisiae. Cell Mol Life Sci *73*, 3115-3136.
Kang, P.J., Hood-DeGrenier, J.K., and Park, H.O. (2013). Coupling of septins to the axial landmark by Bud4 in budding yeast. J Cell Sci *126*, 1218-1226.
Kechad, A., Jananji, S., Ruella, Y., and Hickson, G.R. (2012). Anillin acts as a bifunctional linker coordinating midbody ring biogenesis during cytokinesis. Curr Biol *22*, 197-203.
Kim, M.S., Froese, C.D., Estey, M.P., and Trimble, W.S. (2011). SEPT9 occupies the terminal positions in septin octamers and mediates polymerization-dependent functions in abscission. J Cell Biol *195*, 815-826.
Kinoshita, M., Field, C.M., Coughlin, M.L., Straight, A.F., and Mitchison, T.J. (2002). Self- and actin-templated assembly of Mammalian septins. Dev Cell *3*, 791-802.
Kozubowski, L., Larson, J.R., and Tatchell, K. (2005). Role of the septin ring in the asymmetric localization of proteins at the mother-bud neck in Saccharomyces cerevisiae. Mol Biol Cell *16*, 3455-3466.
Kress, A., Wang, X., Ranchon, H., Savatier, J., Rigneault, H., Ferrand, P., and Brasselet, S. (2013). Mapping the local organization of cell membranes using excitation-polarization-resolved confocal fluorescence microscopy. Biophys J *105*, 127-136.
Lacroix, B., and Maddox, A.S. (2012). Cytokinesis, ploidy and aneuploidy. J Pathol *226*, 338-351.
Lee, I.J., Coffman, V.C., and Wu, J.Q. (2012). Contractile-ring assembly in fission yeast cytokinesis: Recent advances and new perspectives. Cytoskeleton (Hoboken) *69*, 751-763.
Liu, J., Fairn, G.D., Ceccarelli, D.F., Sicheri, F., and Wilde, A. (2012). Cleavage furrow organization requires PIP(2)-mediated recruitment of anillin. Curr Biol *22*, 64-69.
Liu, J., Wang, H., and Balasubramanian, M.K. (2000). A checkpoint that monitors cytokinesis in Schizosaccharomyces pombe. J Cell Sci *113 (Pt 7)*, 1223-1230.

Marquardt, J., Chen, X., and Bi, E. (2019). Architecture, remodeling, and functions of the septin cytoskeleton. Cytoskeleton (Hoboken) *76*, 7-14.
Martin-Cuadrado, A.B., Morrell, J.L., Konomi, M., An, H., Petit, C., Osumi, M., Balasubramanian, M., Gould, K.L., Del Rey, F., and de Aldana, C.R. (2005). Role of septins and the exocyst complex in the function of hydrolytic enzymes responsible for fission yeast cell separation. Mol Biol Cell *16*, 4867-4881.
McCollum, D., and Gould, K.L. (2001). Timing is everything: regulation of mitotic exit and cytokinesis by the MEN and SIN. Trends Cell Biol *11*, 89-95.
McMurray, M.A., and Thorner, J. (2009). Septins: molecular partitioning and the generation of cellular asymmetry. Cell Div *4*, 18.
McQuilken, M., Jentzsch, M.S., Verma, A., Mehta, S.B., Oldenbourg, R., and Gladfelter, A.S. (2017). Analysis of Septin Reorganization at Cytokinesis Using Polarized Fluorescence Microscopy. Front Cell Dev Biol *5*, 42.
Meitinger, F., and Palani, S. (2016). Actomyosin ring driven cytokinesis in budding yeast. Semin Cell Dev Biol *53*, 19-27.
Moreno, S., Klar, A., and Nurse, P. (1991). Molecular genetic analysis of fission yeast Schizosaccharomyces pombe. Methods Enzymol *194*, 795-823.
Mostowy, S., and Cossart, P. (2012). Septins: the fourth component of the cytoskeleton. Nat Rev Mol Cell Biol *13*, 183-194.
Muñoz, M., Cortés, J.C.G., Sipiczki, M., Ramos, M., Clemente-Ramos, J.A., Moreno, M. B., Martins, I.M., Pérez, P., and Ribas, J.C. (2013). Extracellular cell wall β(1,3)glucan is required to couple septation to actomyosin ring contraction. J Cell Biol *203*, 2565-82.
Neufeld, T.P., and Rubin, G.M. (1994). The Drosophila peanut gene is required for cytokinesis and encodes a protein similar to yeast putative bud neck filament proteins. Cell *77*, 371-379.
Oegema, K., Savoian, M.S., Mitchison, T.J., and Field, C.M. (2000). Functional analysis of a human homologue of the Drosophila actin binding protein anillin suggests a role in cytokinesis. J Cell Biol *150*, 539-552.
Ong, K., Wloka, C., Okada, S., Svitkina, T., and Bi, E. (2014). Architecture and dynamic remodelling of the septin cytoskeleton during the cell cycle. Nat Commun *5*, 5698.
Pédelacq, J.D., Cabantous, S., Tran, T., Terwilliger, T.C., and Waldo, G.S. (2006). Engineering and characterization of a superfolder green fluorescent protein. Nat Biotechnol *24*,79-88.
Piekny, A.J., and Glotzer, M. (2008). Anillin is a scaffold protein that links RhoA, actin, and myosin during cytokinesis. Curr Biol *18*, 30-36.
Piekny, A.J., and Maddox, A.S. (2010). The myriad roles of Anillin during cytokinesis. Semin Cell Dev Biol *21*, 881-891.
Pollard, T.D., and Wu, J.Q. (2010). Understanding cytokinesis: lessons from fission yeast. Nat Rev Mol Cell Biol *11*, 149-155.
Ramos, M., Cortés, J.C.G., Sato, M., Rincón, S.A., Moreno, M.B., Clemente-Ramos J.A., Osumi, M., Pérez, P., and Ribas, J.C. (2019). Two S. pombe septation phases differ in ingression rate, septum structure, and response to F-actin loss. J Cell Biol *218*, 4171-4194.
Rincon, S.A., Bhatia, P., Bicho, C., Guzman-Vendrell, M., Fraisier, V., Borek, W.E., Alves Fde, L., Dingli, F., Loew, D., Rappsilber, J.*, et al.* (2014). Pom1 regulates the assembly of Cdr2-Mid1 cortical nodes for robust spatial control of cytokinesis. J Cell Biol *206*, 61-77.
Rincon, S.A., and Paoletti, A. (2012). Mid1/anillin and the spatial regulation of cytokinesis in fission yeast. Cytoskeleton (Hoboken) *69*, 764-777.
Rincon, S.A., and Paoletti, A. (2016). Molecular control of fission yeast cytokinesis. Semin Cell Dev Biol *53*, 28-38.
Saarikangas, J., and Barral, Y. (2011). The emerging functions of septins in metazoans. EMBO Rep *12*, 1118-1126.
Sinha, I., Wang, Y.M., Philp, R., Li, C.R., Yap, W.H., and Wang, Y. (2007). Cyclin-dependent kinases control septin phosphorylation in Candida albicans hyphal development. Dev Cell *13*, 421-432.

Slubowski, C.J., Funk, A.D., Roesner, J.M., Paulissen, S.M., and Huang, L.S. (2015). Plasmids for C-terminal tagging in Saccharomyces cerevisiae that contain improved GFP proteins, Envy and Ivy. Yeast *32*, 379-387.
Somma, M.P., Fasulo, B., Cenci, G., Cundari, E., and Gatti, M. (2002). Molecular dissection of cytokinesis by RNA interference in Drosophila cultured cells. Mol Biol Cell *13*, 2448-2460.
Sparks, C.A., Morphew, M., and McCollum, D. (1999). Sid2p, a spindle pole body kinase that regulates the onset of cytokinesis. J Cell Biol *146*, 777-790.
Storchova, Z., and Pellman, D. (2004). From polyploidy to aneuploidy, genome instability and cancer. Nat Rev Mol Cell Biol *5*, 45-54.
Straight, A.F., Field, C.M., and Mitchison, T.J. (2005). Anillin binds nonmuscle myosin II and regulates the contractile ring. Mol Biol Cell *16*, 193-201.
Surka, M.C., Tsang, C.W., and Trimble, W.S. (2002). The mammalian septin MSF localizes with microtubules and is required for completion of cytokinesis. Mol Biol Cell *13*, 3532-3545.
Tasto, J.J., Morrell, J.L., and Gould, K.L. (2003). An anillin homologue, Mid2p, acts during fission yeast cytokinesis to organize the septin ring and promote cell separation. J Cell Biol *160*, 1093-1103.
Versele, M., and Thorner, J. (2005). Some assembly required: yeast septins provide the instruction manual. Trends Cell Biol *15*, 414-424.
Vrabioiu, A.M., and Mitchison, T.J. (2006). Structural insights into yeast septin organization from polarized fluorescence microscopy. Nature *443*, 466-469.
Wang, X., Kress, A., Brasselet, S., and Ferrand, P. (2013). High frame-rate fluorescence confocal angle-resolved linear dichroism microscopy. Rev Sci Instrum *84*, 053708.
Wloka, C., Nishihama, R., Onishi, M., Oh, Y., Hanna, J., Pringle, J.R., Krauss, M., and Bi, E. (2011). Evidence that a septin diffusion barrier is dispensable for cytokinesis in budding yeast. Biol Chem *392*, 813-829.
Wood, V., Gwilliam, R., Rajandream, M.A., Lyne, M., Lyne, R., Stewart, A., Sgouros, J., Peat, N., Hayles, J., Baker, S*., et al.* (2002). The genome sequence of Schizosaccharomyces pombe. Nature *415*, 871-880.
Wu, H., Guo, J., Zhou, Y.T., and Gao, X.D. (2015). The anillin-related region of Bud4 is the major functional determinant for Bud4's function in septin organization during bud growth and axial bud site selection in budding yeast. Eukaryot Cell *14*, 241-251.
Wu, J.Q., Kuhn, J.R., Kovar, D.R., and Pollard, T.D. (2003). Spatial and temporal pathway for assembly and constriction of the contractile ring in fission yeast cytokinesis. Dev Cell *5*, 723-734.
Wu, J.Q., Ye, Y., Wang, N., Pollard, T.D., and Pringle, J.R. (2010). Cooperation between the septins and the actomyosin ring and role of a cell-integrity pathway during cell division in fission yeast. Genetics *186*, 897-915.
Zhao, W.M., and Fang, G. (2005). Anillin is a substrate of anaphase-promoting complex/cyclosome (APC/C) that controls spatial contractility of myosin during late cytokinesis. J Biol Chem *280*, 33516-33524.
Zheng, S., Dong, F., Rasul, F., Yao, X., Jin, Q.W., Zheng, F., and Fu, C. (2018). Septins regulate the equatorial dynamics of the separation initiation network kinase Sid2p and glucan synthases to ensure proper cytokinesis. FEBS J *285*, 2468-2480.

ABBREVIATIONS

CR: Contractile Ring

SIN: Septation Initiation Network

1 CDK: Cyclin-Dependent Kinase

2 Sd: standard deviation

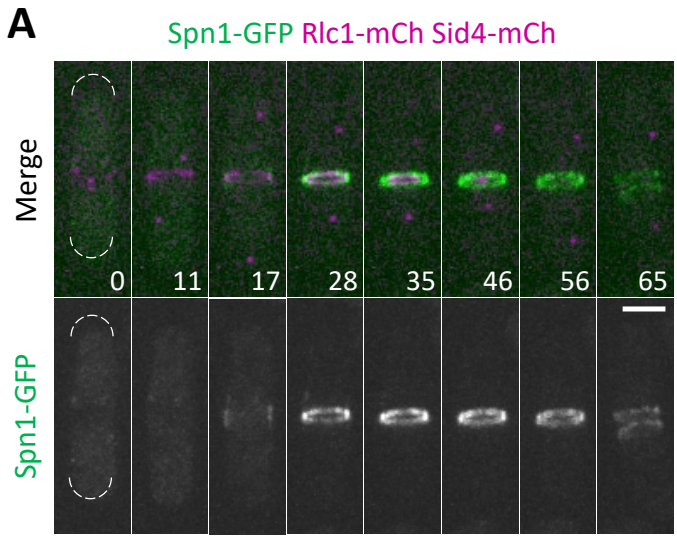
A
Spn1-GFP Rlc1-mCh Sid4-mCh
Merge
Spn1-GFP
0
11
17
28
35
46
56
65

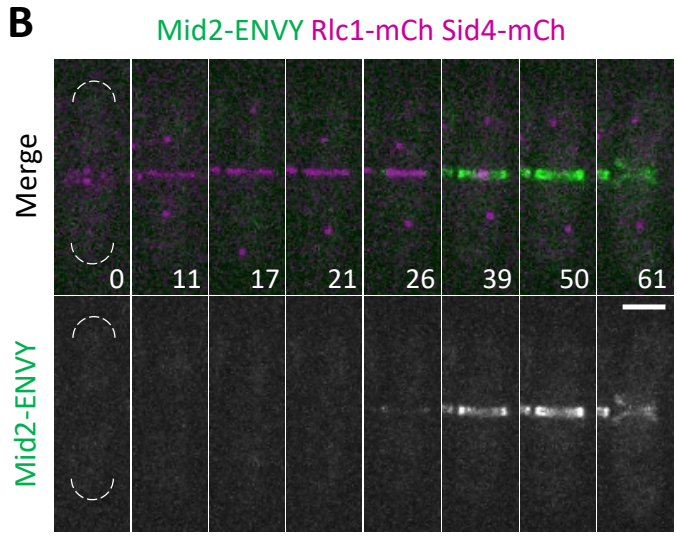
B
Mid2-ENVY Rlc1-mCh Sid4-mCh
Merge
Mid2-ENVY
0
11
17
21
26
39
50
61

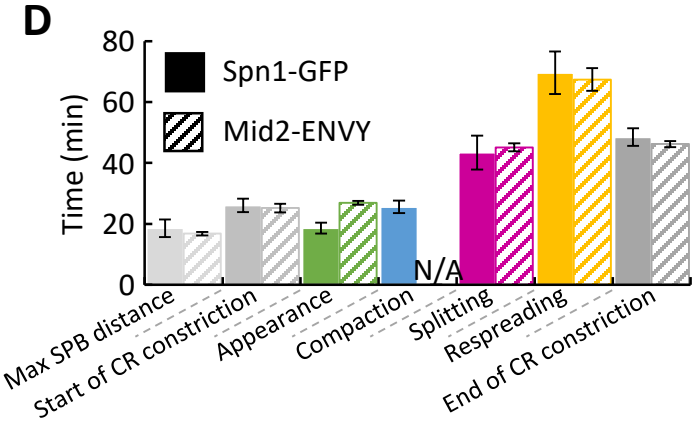
D
Time (min)
80
60
40
20
0
Spn1-GFP
Mid2-ENVY
N/A
Max SPB distance
Start of CR constriction
Appearance
Compaction
Splitting
Respreading
End of CR constriction

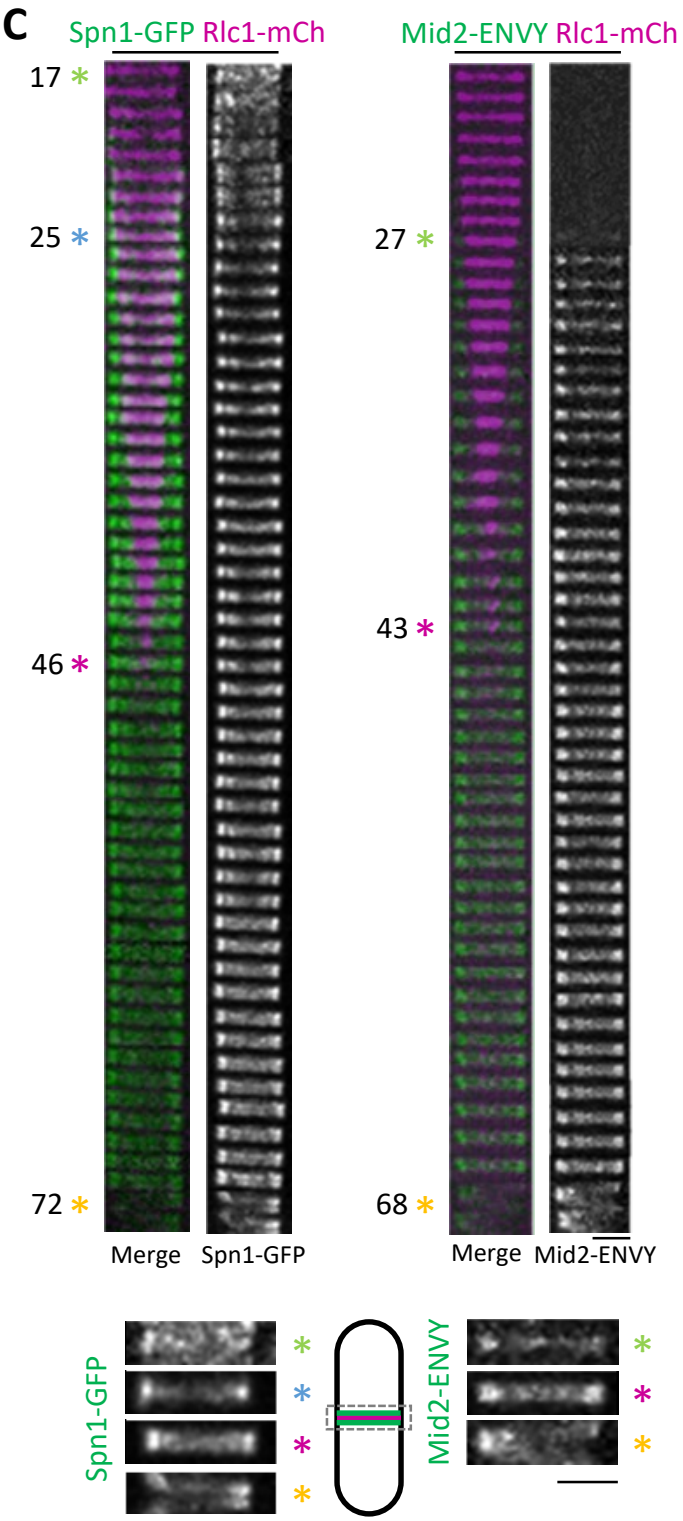
C
Spn1-GFP Rlc1-mCh
Mid2-ENVY Rlc1-mCh
17
25
46
72
27
43
68
Merge
Spn1-GFP
Merge
Mid2-ENVY
Spn1-GFP
Mid2-ENVY

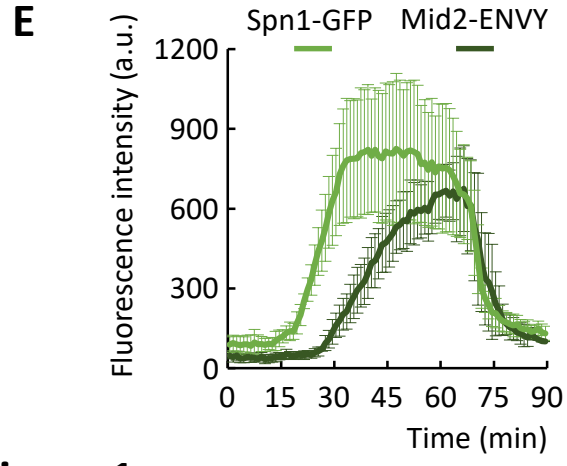
E
Spn1-GFP
Mid2-ENVY
Fluorescence intensity (a.u.)
1200
900
600
300
0
0
15
30
45
60
75
90
Time (min)

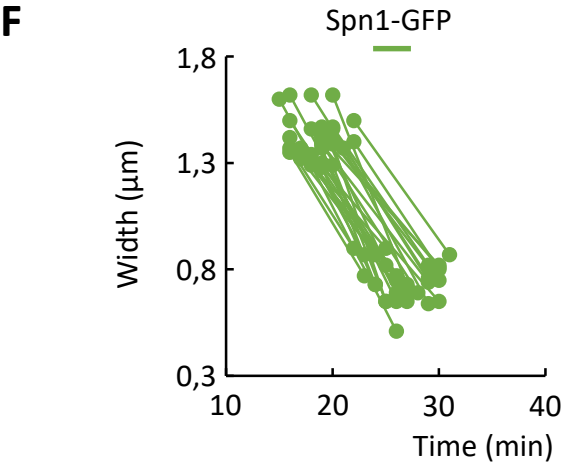
F
Spn1-GFP
Width (µm)
1,8
1,3
0,8
0,3
10
20
30
40
Time (min)

Figure 1

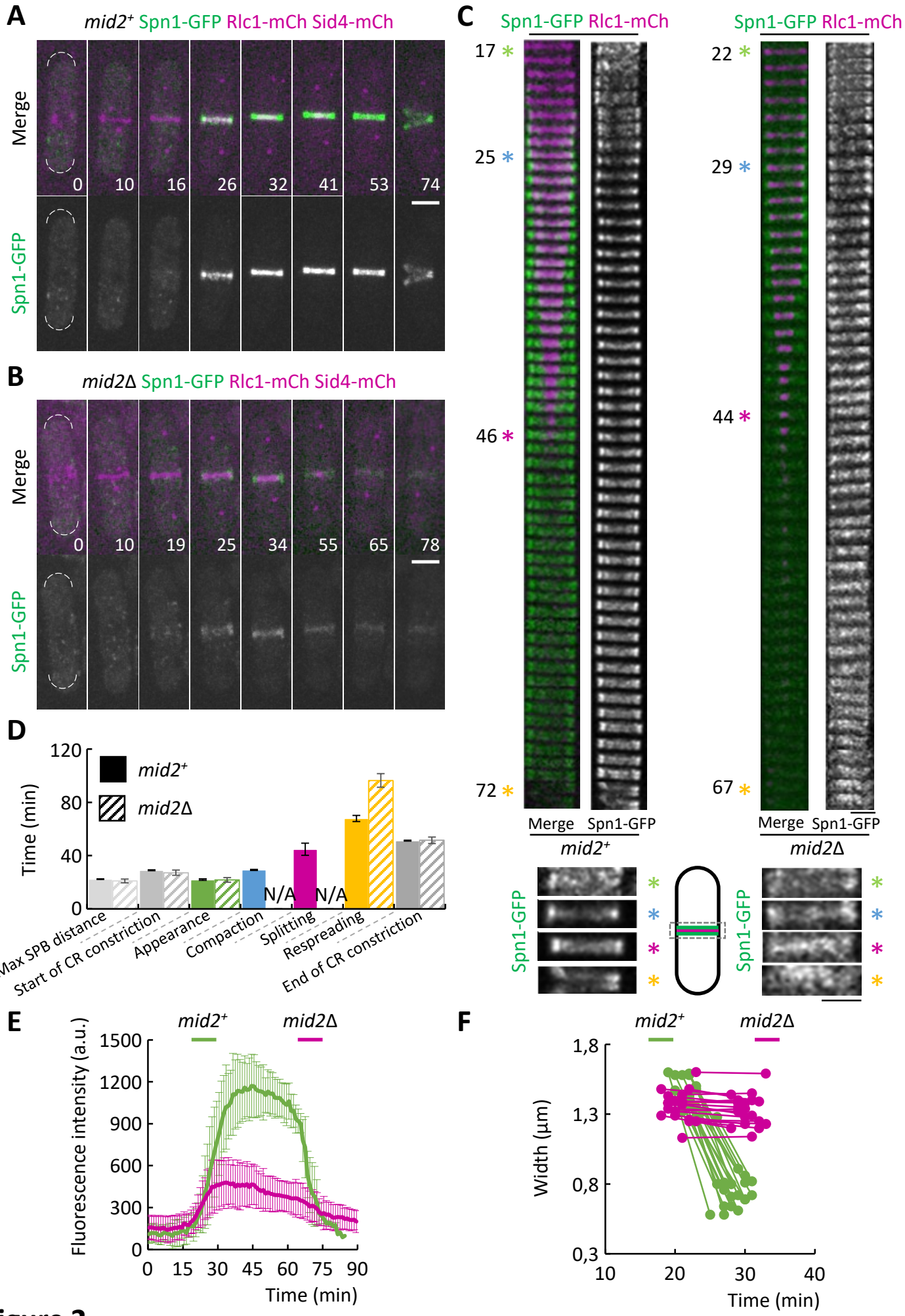
A
mid2⁺ Spn1-GFP Rlc1-mCh Sid4-mCh
Merge
Spn1-GFP
0
10
16
26
32
41
53
74
B
mid2Δ Spn1-GFP Rlc1-mCh Sid4-mCh
Merge
Spn1-GFP
0
10
19
25
34
55
65
78
C
Spn1-GFP Rlc1-mCh
17
25
46
72
22
29
44
67
Merge
Spn1-GFP
mid2⁺
mid2Δ
D
Time (min)
120
80
40
0
mid2⁺
mid2Δ
N/A
N/A
Max SPB distance
Start of CR constriction
Appearance
Compaction
Splitting
Respreading
End of CR constriction
E
mid2⁺
mid2Δ
Fluorescence intensity (a.u.)
1500
1200
900
600
300
0
0
15
30
45
60
75
90
Time (min)
F
mid2⁺
mid2Δ
Width (µm)
1,8
1,3
0,8
0,3
10
20
30
40
Time (min)

Figure 2

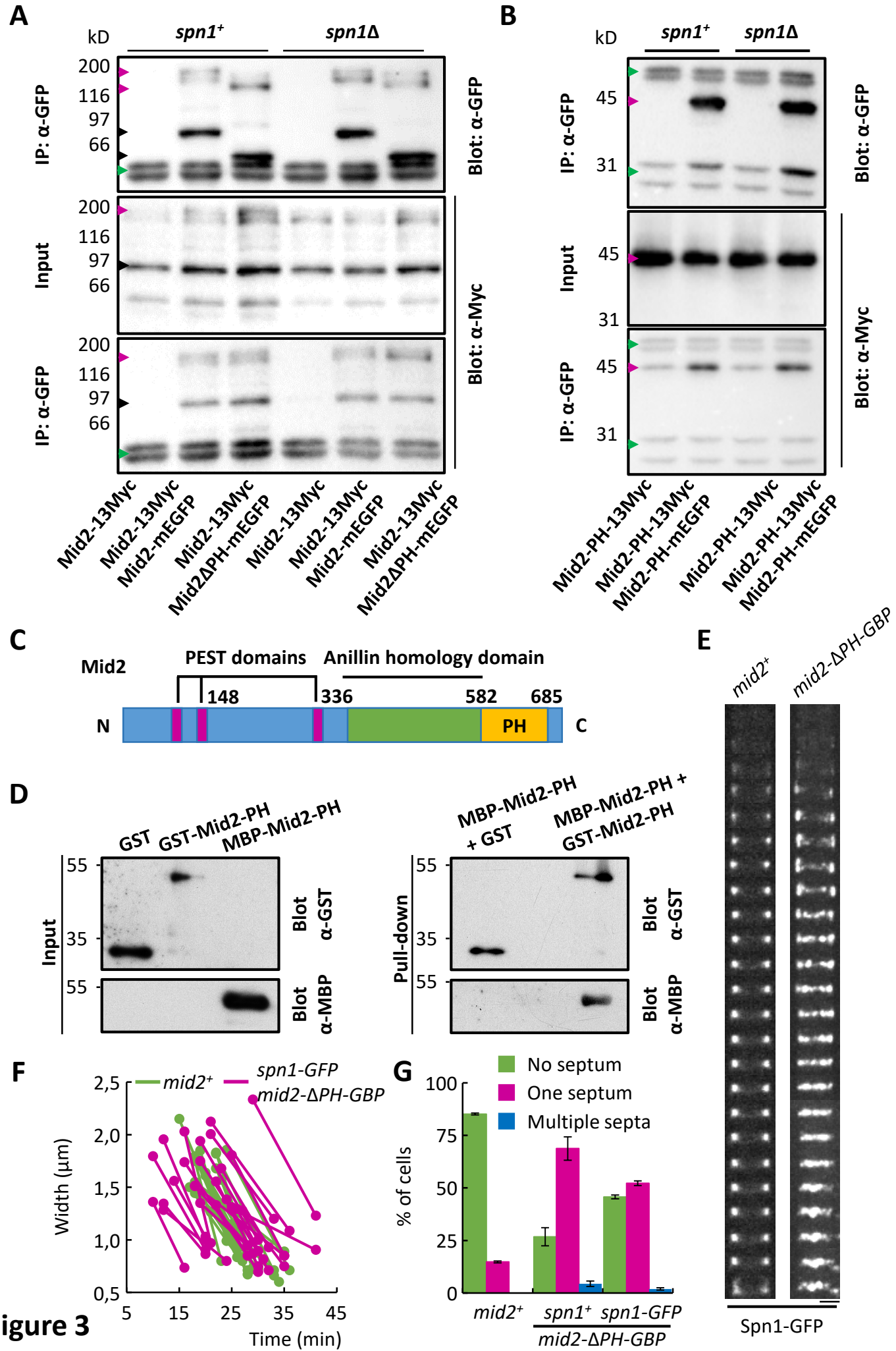
A
kD
spn1+
spn1Δ
200
116
97
66
IP: α-GFP
Input
IP: α-GFP
Blot: α-GFP
Blot: α-Myc
Mid2-13Myc
Mid2-13Myc
Mid2-mEGFP
Mid2-13Myc
Mid2ΔPH-mEGFP
Mid2-13Myc
Mid2-13Myc
Mid2-mEGFP
Mid2-13Myc
Mid2ΔPH-mEGFP
B
kD
spn1+
spn1Δ
45
31
IP: α-GFP
Input
IP: α-GFP
Blot: α-GFP
Blot: α-Myc
Mid2-PH-13Myc
Mid2-PH-13Myc
Mid2-PH-mEGFP
Mid2-PH-13Myc
Mid2-PH-13Myc
Mid2-PH-mEGFP
C
Mid2
PEST domains
Anillin homology domain
148
336
582
685
N
PH
C
D
GST
GST-Mid2-PH
MBP-Mid2-PH
MBP-Mid2-PH + GST
MBP-Mid2-PH + GST-Mid2-PH
55
35
55
Input
Pull-down
Blot α-GST
Blot α-MBP
E
mid2+
mid2-ΔPH-GBP
Spn1-GFP
F
mid2+
spn1-GFP
mid2-ΔPH-GBP
2,5
2,0
1,5
1,0
0,5
Width (μm)
5
15
25
35
45
Time (min)
G
No septum
One septum
Multiple septa
100
75
50
25
0
% of cells
mid2+
spn1+
spn1-GFP
mid2-ΔPH-GBP

Figure 3

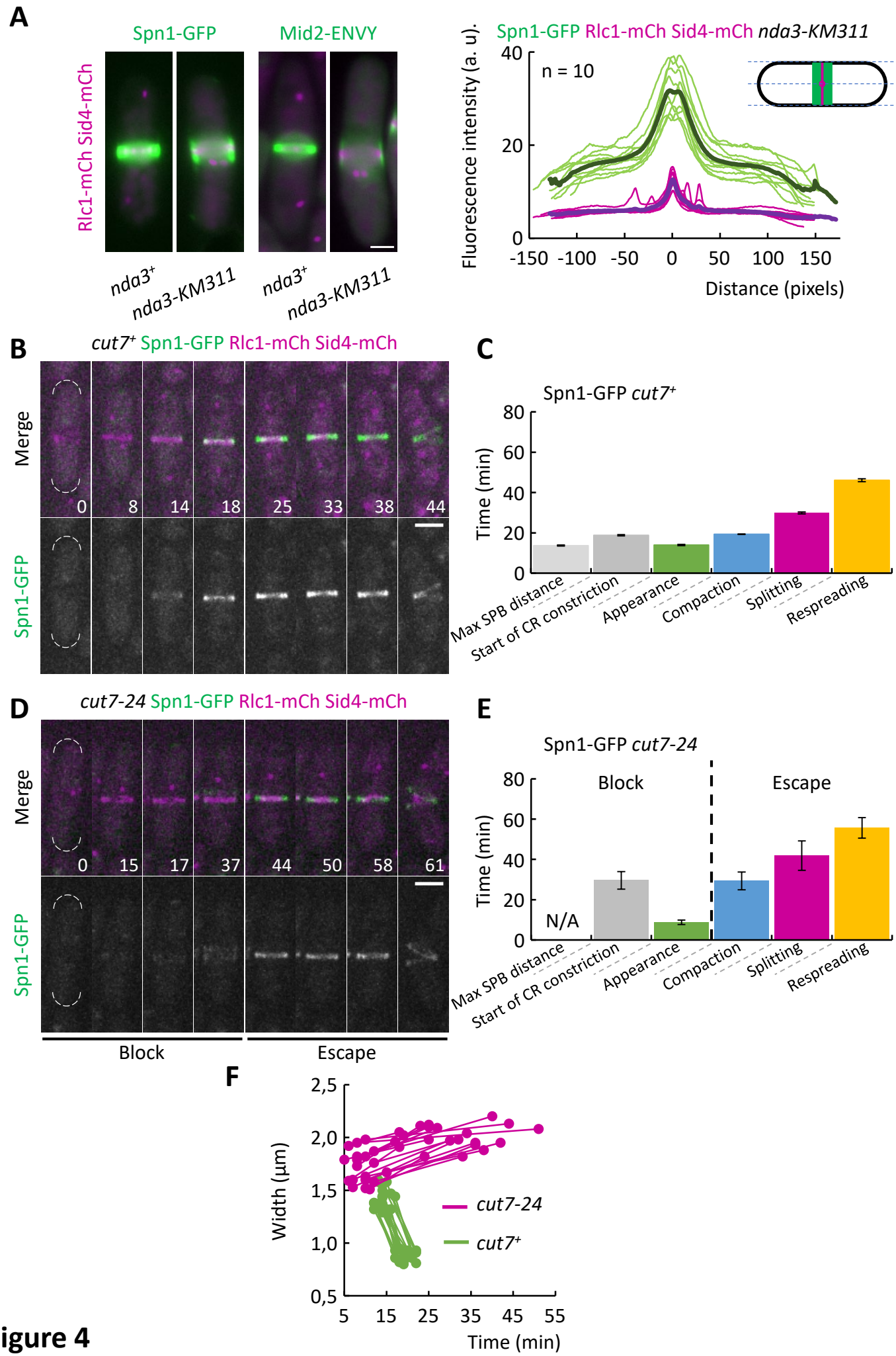
A
Spn1-GFP
Mid2-ENVY
Rlc1-mCh Sid4-mCh
nda3+
nda3-KM311
nda3+
nda3-KM311
Spn1-GFP Rlc1-mCh Sid4-mCh nda3-KM311
n = 10
Fluorescence intensity (a. u.)
Distance (pixels)
B
cut7+ Spn1-GFP Rlc1-mCh Sid4-mCh
Merge
Spn1-GFP
C
Spn1-GFP cut7+
Time (min)
Max SPB distance
Start of CR constriction
Appearance
Compaction
Splitting
Respreading
D
cut7-24 Spn1-GFP Rlc1-mCh Sid4-mCh
Block
Escape
E
Spn1-GFP cut7-24
N/A
F
Width (µm)
cut7-24
cut7+
Time (min)

Figure 4

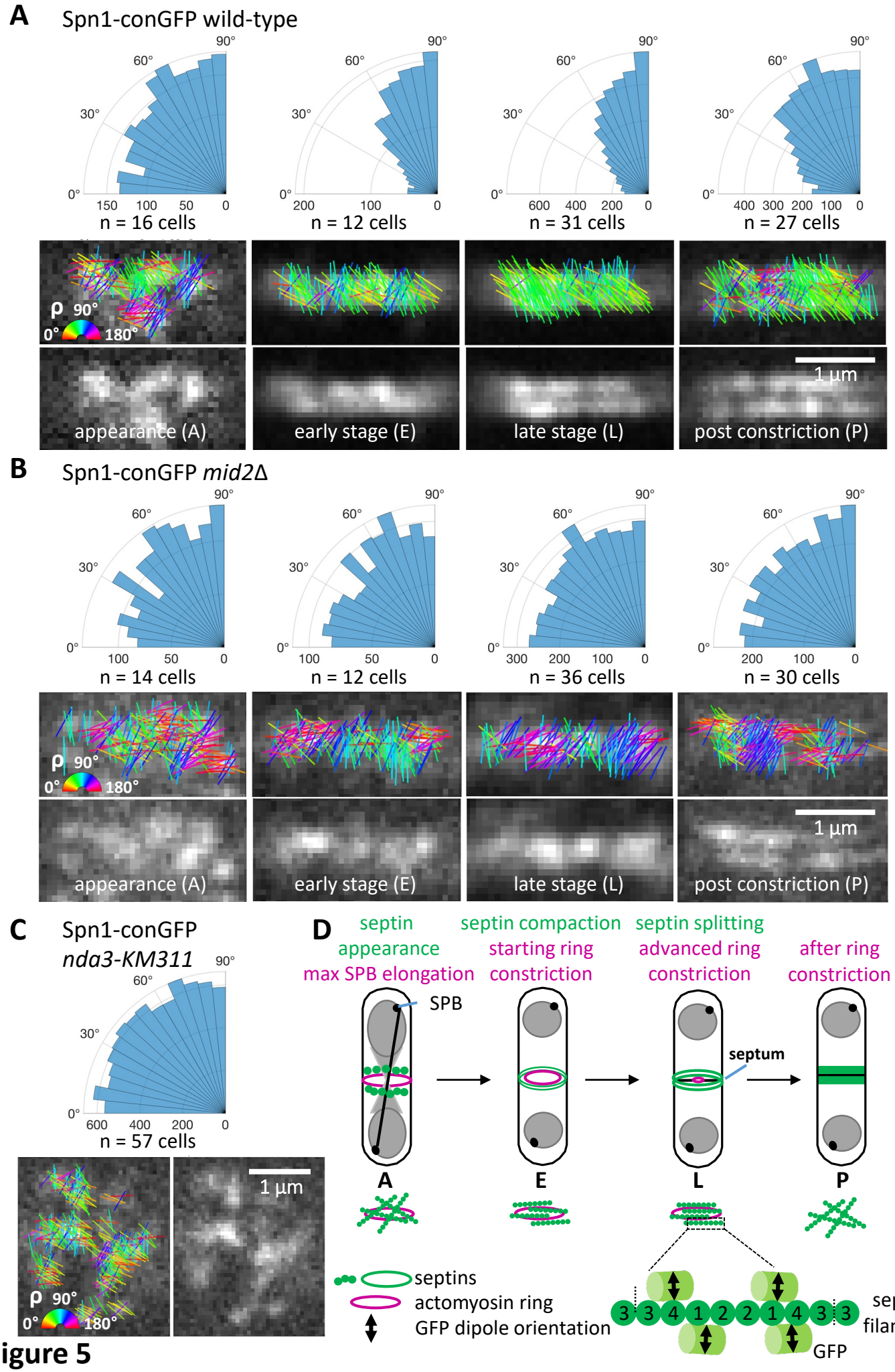
A
Spn1-conGFP wild-type
n = 16 cells
n = 12 cells
n = 31 cells
n = 27 cells
ρ 90°
0° 180°
1 µm
appearance (A)
early stage (E)
late stage (L)
post constriction (P)
B
Spn1-conGFP mid2Δ
n = 14 cells
n = 12 cells
n = 36 cells
n = 30 cells
ρ 90°
0° 180°
1 µm
appearance (A)
early stage (E)
late stage (L)
post constriction (P)
C
Spn1-conGFP
nda3-KM311
n = 57 cells
ρ 90°
0° 180°
1 µm
D
septin appearance
max SPB elongation
septin compaction
starting ring constriction
septin splitting
advanced ring constriction
after ring constriction
SPB
septum
A
E
L
P
septins
actomyosin ring
GFP dipole orientation
septin filament
GFP

Figure 5

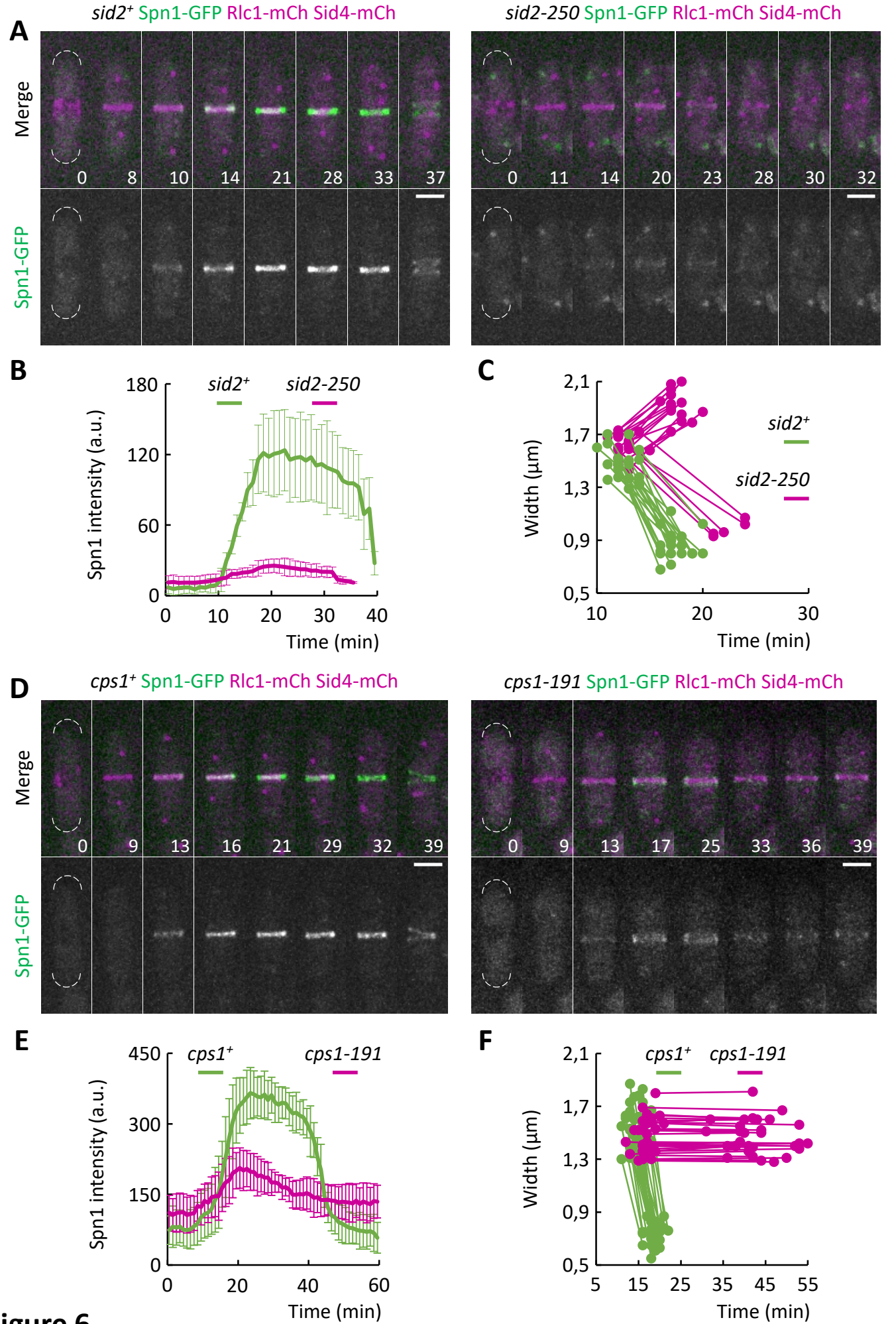
A
sid2+ Spn1-GFP Rlc1-mCh Sid4-mCh
sid2-250 Spn1-GFP Rlc1-mCh Sid4-mCh
Merge
Spn1-GFP
0 8 10 14 21 28 33 37
0 11 14 20 23 28 30 32
B
Spn1 intensity (a.u.)
sid2+
sid2-250
180
120
60
0
0 10 20 30 40
Time (min)
C
Width (µm)
2,1
1,7
1,3
0,9
0,5
sid2+
sid2-250
10 20 30
Time (min)
D
cps1+ Spn1-GFP Rlc1-mCh Sid4-mCh
cps1-191 Spn1-GFP Rlc1-mCh Sid4-mCh
Merge
Spn1-GFP
0 9 13 16 21 29 32 39
0 9 13 17 25 33 36 39
E
Spn1 intensity (a.u.)
cps1+
cps1-191
450
300
150
0
0 20 40 60
Time (min)
F
Width (µm)
cps1+
cps1-191
2,1
1,7
1,3
0,9
0,5
5 15 25 35 45 55
Time (min)

Figure 6

SUPPLEMENTAL INFORMATION

Table S1. Table of strains used in this study.

Strain	Genotype	Source
Figure 1		
AP5501	*spn1-GFP:kanMX6 rlc1-mCherry:natMX6 sid4-mCherry:hphMX6 ade6- ura4-D18 leu1-32*	This study
AP5678	*mid2-ENVY:kanMX6 rlc1-mCherry:natMX6 sid4-mCherry:hphMX6 ade6- ura4-D18 leu1-32*	This study
Figure 2		
AP5501	*spn1-GFP:kanMX6 rlc1-mCherry:natMX6 sid4-mCherry:hphMX6 ade6- ura4-D18 leu1-32*	This study
AP5582	*spn1-GFP:kanMX6 mid2Δ::kanMX6 rlc1-mCherry:natMX6 sid4-mCherry:hphMX6 ade6- ura4-D18 leu1-32*	This study
Figure 3		
AP5823	*mid2-13xMyc:Nat ade6-M210 ura4-D18 leu1-32*	This study
AP5831	*leu1+:Pmid2-mid2-mEGFP mid2-13xMyc:Nat ade6- ura4-D18 leu1-32*	This study
AP5829	*leu1+:Pmid2-mid2ΔPH-mEGFP mid2-13xMyc:Nat ade6- ura4-D18 leu1-32*	This study
AP5918	*spn1Δ::ura4+ mid2-13xMyc:Nat ade6- ura4-D18 leu1-32*	This study
AP5920	*spn1Δ::ura4+ leu1+:Pmid2-mid2-mEGFP mid2-13xMyc:natMX6 ade6-*	This study
AP5927	*spn1Δ::ura4+ leu1+:Pmid2-mid2ΔPH-mEGFP mid2-13xMyc:natMX6 ade6- ura4-D18 leu1-32*	This study
AP5814	*leu1+:Pmid2-mid2-PH-13xMyc ade6- ura4-D18 leu1-32*	This study
AP5932	*mid2-PH-mEGFP:kanMX6 leu1+:Pmid2-mid2-PH-13xMyc ade6- ura4-D18 leu1-32*	This study
AP5930	*spn1Δ::ura4+ leu1+:Pmid2-mid2-PH-13xMyc ade6- ura4-D18 leu1-32*	This study
AP5943	*spn1Δ::ura4+ mid2-PH-mEGFP:kanMX6 leu1+:Pmid2-mid2-PH-13xMyc ade6- ura4-D18 leu1-32*	This study
SR1370	*mid2Δ::mEGFP:kanMX6 ade6: :Pmid2-mid2-PH-13xMyc ade6- ura4-D18 leu1-32*	This study
AP5501	*spn1-GFP:kanMX6 rlc1-mCherry:natMX6 sid4-mCherry:hphMX6 ade6- ura4-D18 leu1-32*	This study

SR1216	*mid2-ΔPH-GBP:kanMX6 spn1-GFP:hphMX6 rlc1-mCherry:natMX6 sid4-mCherry:hphMX6 ade6- ura4-D18 leu1-32*	This study
SR1210	*mid2-ΔPH-GBP:kanMX6 rlc1-mCherry:natMX6 sid4-mCherry:hphMX6 ade6- ura4-D18 leu1-32*	This study
Figure 4		
AP5501	*spn1-GFP:kanMX6 rlc1-mCherry:natMX6 sid4-mCherry:hphMX6 ade6- ura4-D18 leu1-32*	This study
AP5515	*spn1-GFP:kanMX6 rlc1-mCherry:natMX6 sid4-mCherry:hphMX6 nda3-KM311 ade6- ura4-D18 leu1-32*	This study
AP6268	*spn1-GFP:kanMX6 rlc1-mCherry:natMX6 sid4-mCherry:hphMX6 cut7-24 ade6- ura4-D18 leu1-32*	This study
AP5678	*mid2-ENVY:kanMX6 rlc1-mCherry:natMX6 sid4-mCherry:hphMX6 ade6- ura4-D18 leu1-32*	This study
AP5514	*mid2-ENVY:kanMX6 rlc1-mCherry:natMX6 sid4-mCherry:hphMX6 nda3-KM311 ade6- ura4-D18 leu1-32*	This study
Figure 5		
AP6313	*spn1-msfGFPΔN12:kanMX6 rlc1-mCherry:natMX6 sid4-mCherry:hphMX6 ade6- ura4-D18 leu1-32*	This study
AP6334	*spn1-msfGFPΔN12:kanMX6 mid2::hphMX6 rlc1-mCherry:natMX6 sid4-mCherry:hphMX6 ade6- ura4-D18 leu1-32*	This study
AP6324	*spn1-msfGFPΔN12:kanMX6 nda3-KM311 rlc1-mCherry:natMX6 sid4-mCherry:hphMX6 ade6- ura4-D18 leu1-32*	This study
Figure 6		
AP5501	*spn1-GFP:kanMX6 rlc1-mCherry:natMX6 sid4-mCherry:hphMX6 ade6- ura4-D18 leu1-32*	This study
AP5585	*spn1-GFP:kanMX6 rlc1-mCherry:natMX6 sid4-mCherry:hphMX6 sid2-250 ade6- ura4-D18 leu1-32*	This study
AP5633	*spn1-GFP:kanMX6 rlc1-mCherry:natMX6 sid4-mCherry:hphMX6 cps1-191 ade6- ura4-D18 leu1-32*	This study
Figure S1		
AP5501	*spn1-GFP:kanMX6 rlc1-mCherry:natMX6 sid4-mCherry:hphMX6 ade6- ura4-D18 leu1-32*	This study
AP5582	*spn1-GFP:kanMX6 mid2Δ::kanMX6 rlc1-mCherry:natMX6 sid4-mCherry:hphMX6 ade6- ura4-D18 leu1-32*	This study
AP5823	*mid2-13xMyc:Nat ade6-M210 ura4-D18 leu1-32*	This study

AP6274	*mid2-13xMyc:natMX6 nda3-KM311 ade6- ura4-D18 leu1-32*	This study
AP6276	*spn1-GFP:KanMX6 mid2-13XMyc:natMX6 ura4-D18 leu1-32*	This study
AP6280	*spn1-GFP:KanMX6 mid2-13XMyc:natMX6 nda3-KM311 ura4-D18 leu1-32*	This study
Figure S2		
AP6274	*mid2-13xMyc:natMX6 nda3-KM311 ade6- ura4-D18 leu1-32*	This study
AP6069	*leu1+:Pmid2-mid2-mEGFP mid2-13xMyc:natMX6 nda3-KM311 ade6- ura4-D18 leu1-32*	This study
AP6073	*leu1+:Pmid2-mid2ΔPH-mEGFP mid2-13xMyc:natMX6 nda3-KM311 ade6- ura4-D18 leu1-32*	This study
AP6074	*leu1+:Pmid2-mid2-PH-mEGFP mid2-13Myc:natMX6 nda3-KM311 ade6- ura4-D18 leu1-32*	This study
SR1344	*mid2-mEGFP:kanMX6 ade6:mid2-13xMyc ade6- ura4-D18 leu1-32*	This study
SR1234	*spn1-5Δ::ura4+ mid2-mEGFP:kanMX6 ade6:mid2-13xMyc ade6- ura4-D18*	This study
SR1346	*mid2-ΔPH-mEGFP:kanMX6 ade6:mid2-13xMyc ade6- ura4-D18 leu1-32*	This study
SR1236	*spn1-5Δ::ura4+ mid2-ΔPH-mEGFP:kanMX6 ade6:mid2-13xMyc ade6- ura4-D18*	This study
SR1348	*PH-mid2-mEGFP:kanMX6 ade6: PH-mid2-13xMyc ade6- ura4-D18 leu1-32*	This study
SR1237	*spn1-5Δ::ura4+ PH-mid2-mEGFP:kanMX6 ade6: PH-mid2-13xMyc ade6- ura4-D18*	This study
Figure S3		
AP5678	*mid2-ENVY:kanMX6 rlc1-mCherry:natMX6 sid4-mCherry:hphMX6 ade6- ura4-D18 leu1-32*	This study
AP6271	*mid2-ENVY:kanMX6 rlc1-mCherry:natMX6 sid4-mCherry:hphMX6 cut7-24 ade6- ura4-D18 leu1-32*	This study
AP5501	*spn1-GFP:kanMX6 rlc1-mCherry:natMX6 sid4-mCherry:hphMX6 ade6- ura4-D18 leu1-32*	This study
AP5515	*spn1-GFP:kanMX6 rlc1-mCherry:natMX6 sid4-mCherry:hphMX6 nda3-KM311 ade6- ura4-D18 leu1-32*	This study
AP5678	*mid2-ENVY:kanMX6 rlc1-mCherry:natMX6 sid4-mCherry:hphMX6 ade6- ura4-D18 leu1-32*	This study

AP5514	*mid2-ENVY:kanMX6 rlc1-mCherry:natMX6 sid4-mCherry:hphMX6 nda3-KM311 ade6- ura4-D18 leu1-32*	This study
Figure S4		
AP5501	*spn1-GFP:kanMX6 rlc1-mCherry:natMX6 sid4-mCherry:hphMX6 ade6- ura4-D18 leu1-32*	This study
AP6313	*spn1-msfGFPΔN12:kanMX6 rlc1-mCherry:natMX6 sid4-mCherry:hphMX6 ade6- ura4-D18 leu1-32*	This study
AP6334	*spn1-msfGFPΔN12:kanMX6 mid2::hphMX6 rlc1-mCherry:natMX6 sid4-mCherry:hphMX6 ade6- ura4-D18 leu1-32*	This study
AP6324	*spn1-msfGFPΔN12:kanMX6 nda3-KM311 rlc1-mCherry:natMX6 sid4-mCherry:hphMX6 ade6- ura4-D18 leu1-32*	This study
AP6234	*spn4ΔC6-msfGFPΔN7:kanMX6 rlc1-mCherry:natMX6 sid4-mCherry:hphMX6 ade6- ura4-D18 leu1-32*	This study
Figure S5		
AP5678	*mid2-ENVY:kanMX6 rlc1-mCherry:natMX6 sid4-mCherry:hphMX6 ade6- ura4-D18 leu1-32*	This study
AP5564	*mid2-ENVY:kanMX6 rlc1-mCherry:natMX6 sid4-mCherry:hphMX6 sid2-250 ade6- ura4-D18 leu1-32*	This study
AP5855	*mid2-ENVY:kanMX6 rlc1-mCherry:natMX6 sid4-mCherry:hphMX6 cps1-191 ade6- ura4-D18 leu1-32*	This study

SUPPLEMENTAL FIGURE LEGENDS

Figure S1: Septin compaction is defective in *mid2*Δ cells, and Mid2 and septins interact in *nda3-KM311*-blocked cells and Mid2 self-interaction is septin independent

A: Kymographs of the lateral region of the medial cortex (indicated in the scheme at the bottom) of wild type (left) or *mid2*Δ cells (right) producing Spn1-GFP, Rlc1-mCherry and Sid4-mCherry. Elapsed time is shown in minutes. The major transitions in the behavior of Spn1 from mitosis onset and the defects observed in the absence of Mid2 are highlighted in magnified panels at the far right and indicated with a color-coded asterisk that matches that of the kymograph in figure 1C. **B:** Co-immunoprecipitation assay between Mid2-13XMyc and Spn1-GFP in control and *nda3-KM311* cells incubated at 18°C for 7 hours (lanes 1, 2, 3 and 4) and released for 1 hour at 25°C (lanes 5, 6, 7 and 8). Magenta arrowheads show the expected Spn1 or Mid2 bands; black arrowheads show degradation products; green arrowheads depict the immunoglobulin bands.

Figure S2: The PH domain of Mid2 self-interacts in two hybrid assays and Mid2 co-immunoprecipitates with itself in *nda3-KM311*-blocked cells

A: Co-immunoprecipitation assay between full length Mid2-13Myc and Mid2-mEGFP or Mid2 ΔPH -13Myc and Mid2ΔPH-GFP either in the presence (wt) or in the absence of septins (*spn1-5*Δ). Magenta arrowheads show the expected Mid2 bands; black arrowheads show degradation products. **B:** Co-immunoprecipitation assay between the PH domain of Mid2 tagged with 13XMyc and the PH domain of Mid2 tagged with GFP either in the presence (wt) or in the absence of septins (*spn1-5*Δ).**C:** Two-hybrid assay showing the interaction of the PH domain of Mid2 with itself. The serially diluted growth of the indicated transformants is shown under non-selective (left panel) or selective conditions (right panel). **D:** Co-immunoprecipitation assay between Mid2-13XMyc and full length Mid2-GFP, Mid2ΔPH-GFP or the PH domain of Mid2 tagged with GFP in *nda3-KM311* cells incubated at 18°C for 8 hours. Magenta arrowheads show the expected Mid2 bands; black arrowheads show degradation products; green arrowheads depict the immunoglobulin bands.

Figure S3: Under high CDK activity, septins and Mid2 appear as a broad band at both sides of the CR

Fluorescence intensity analysis of Spn1-GFP, Rlc1-mcherry and Sid4-mcherry signal measured along the entire cell in epifluorescence images of the *nda3-KM311* mutant incubated at 18°C for 8 hours in a representative cell where the SPBs are aligned (**A**) or not (**B**) with respect to the ring position. **C:** Quantification of Spn1-GFP and Mid2-ENVY width over time in wild type (light green for Spn1-GFP and dark green for Mid2-ENVY) and *nda3-KM311* mutant cells (magenta for Spn1-GFP and purple for Mid2-ENVY) incubated at 18°C during 8 hours. The last data point has been taken after switching the cells to 25°C for 1 hour. The average curves ± sd are displayed. n>500 cells. Time lapse imaging of wild type (**D**) or *cut7-24* cells (**F**) expressing Mid2-ENVY, Rlc1-mcherry and Sid4-mcherry incubated at 36°C for 3 hours. Maximum intensity projections of confocal images are shown. Time 0 corresponds to mitotic entry. Scale bars: 2 µm. Plot displaying Mid2-ENVY dynamics throughout cell division in control (**E**) and *cut7-24* cells (**G**). Mean ± sd are shown. n=45 cells in each strain. **H:** Quantification of the extent of Mid2-ENVY width compaction over time in wild type (dark green) and *cut7-24* cells (purple). n=20 cells in each case.

Figure S4: Localization and orientation measurements of Spn1-conGFP and Spn4-conGFP in wild type cells

A: Polar-plot histograms of GFP dipole orientations of Spn1-GFP filaments from wild type cells at different stages of cytokinesis (top panels). The number of analyzed cells per stage is indicated below each polar-plot histogram. Confocal grayscale images of Spn1-GFP from selected wild type cells and an overlaid color-coded stick representation of the measured orientations (angles ρ) per analyzed pixel at each cytokinetic stage (bottom panels). The mean orientation of GFP dipoles per pixel is represented as a stick whose orientation and color are the measured angle ρ. Scale bar: 1 µm. **B**: Maximum intensity projection images of Spn1-GFP, Rlc1-mCherry and Sid4-mCherry in wild type cells (left) and Spn1-conGFP, Rlc1-mCherry and Sid4-

mCherry (right) in wild type, *mid2*Δ and *nda3-KM311* cells at each stage of cytokinesis. Representative large field-of-view maximum intensity projection images of wild type *rlc1-mCherry sid4-mCherry* cells producing Spn1-conGFP (**C**) or Spn4-conGFP (**D**) used for binning cells in each cytokinetic stage before polarimetry measurements. White asterisks in the insets in (D) point to septin rings in selected cells (outlined rectangles), while white arrows point to ectopic cytoplasmic bar-like structures upon Spn4-conGFP production. Scale bars: 10 µm. An example of a polar plot of dipole orientations in a Spn4-conGFP bar-like structure is shown on the right. A confocal grayscale image of the bar-like structure and an overlaid color-coded stick representation of the measured orientations in this structure are shown below the polar-plot histogram. Scale bar: 1 µm. **E:** Examples of cells with Spn4-conGFP in septin rings during CR constriction (left) and during early stages of post constriction (right). Confocal grayscale images of selected cells are shown together with the respective overlaid color-coded stick representation of the measured orientations and the corresponding polar-plot histograms.

Figure S5: Mid2 recruitment to the division region is compromised under low SIN activity or in the β(1,3)-glucan synthase Bgs1 mutant *cps1-191*

A: Time lapse imaging of wild type (left series) and *sid2-250* cells (right series) producing Mid2-ENVY, Rlc1-mCherry and Sid4-mCherry incubated at 36°C for 3 hours. Maximum intensity projections of confocal images are shown. Time 0 corresponds to mitotic entry. Scale bars: 2 µm. **B:** Analysis of Mid2-ENVY fluorescence intensity from mitotic onset throughout cell division in control (dark green) and *sid2-250* cells (purple). The average line graphics ± sd are displayed. n=6 cells in each case. **C:** Time lapse imaging of wild type (left series) and *cps1-191* cells (right series) producing Mid2-ENVY, Rlc1-mCherry and Sid4-mCherry incubated at 36°C for 3 hours. Maximum intensity projections of confocal images are shown. Time 0 corresponds to mitotic entry. Scale bars: 2 µm. **D:** Analysis of Mid2-ENVY fluorescence intensity from mitotic onset throughout cell division in control (dark green) and *cps1-191* cells (purple). The average line graphics ± sd are displayed. n=6 cells in each case.

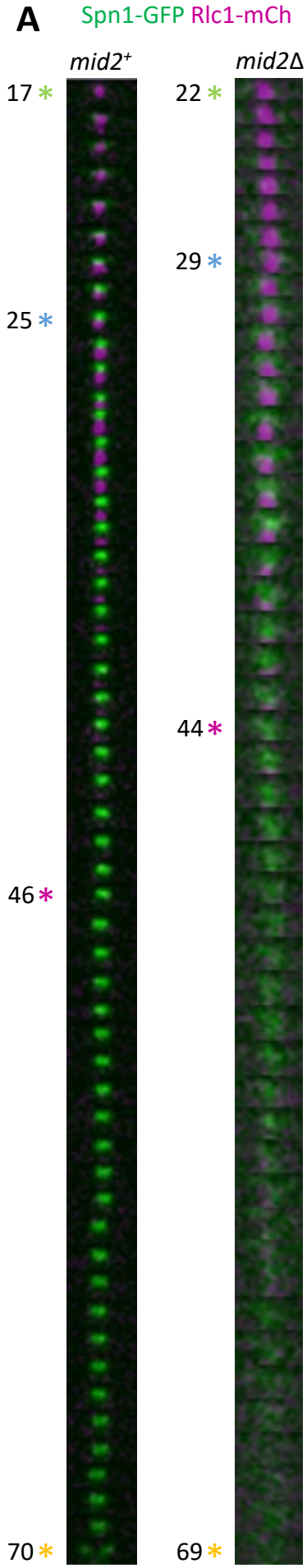
A
Spn1-GFP Rlc1-mCh
mid2+
mid2Δ
17
22
29
25
44
46
70
69

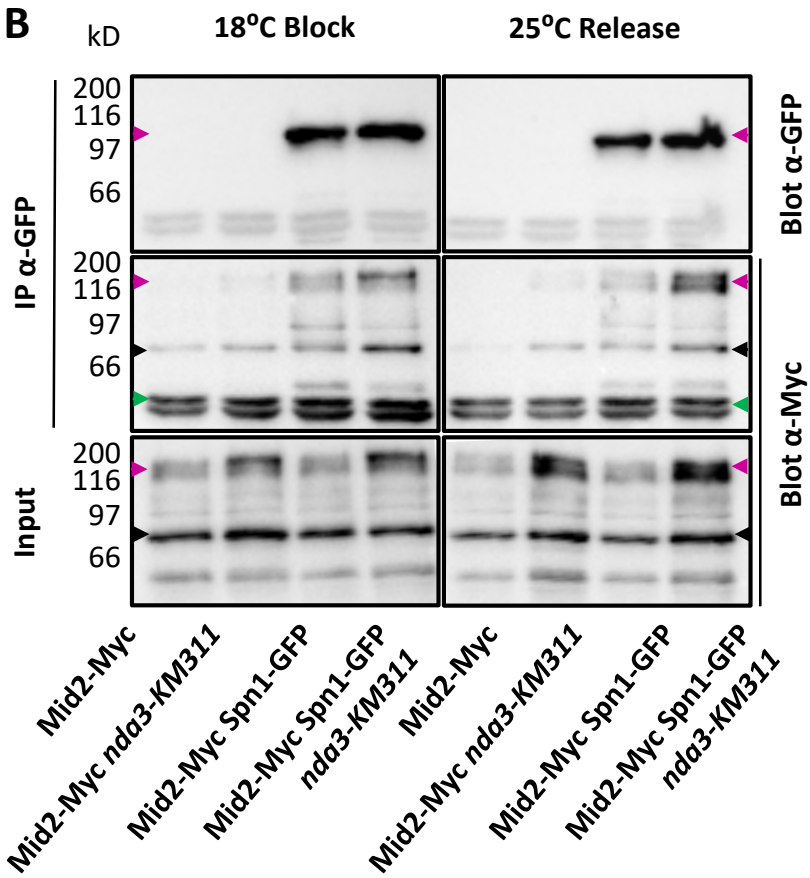
B
kD
18°C Block
25°C Release
200
116
97
66
IP α-GFP
Input
Blot α-GFP
Blot α-Myc
Mid2-Myc
Mid2-Myc nda3-KM311
Mid2-Myc Spn1-GFP
Mid2-Myc Spn1-GFP nda3-KM311

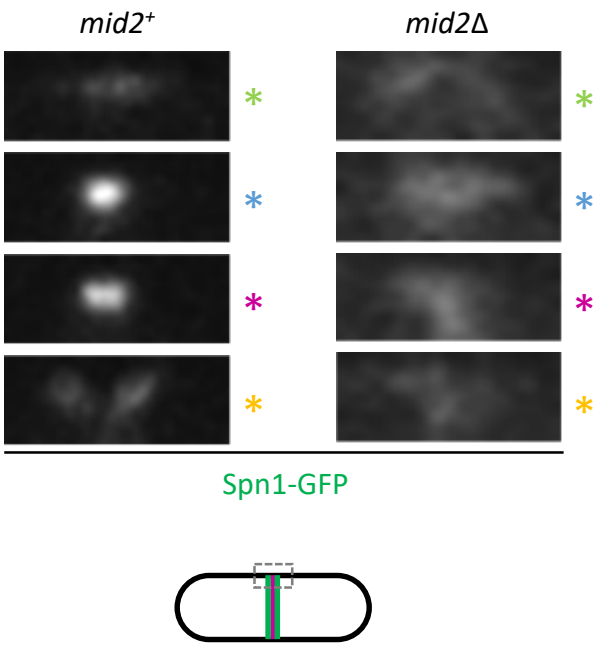
mid2+
mid2Δ
Spn1-GFP

Figure S1

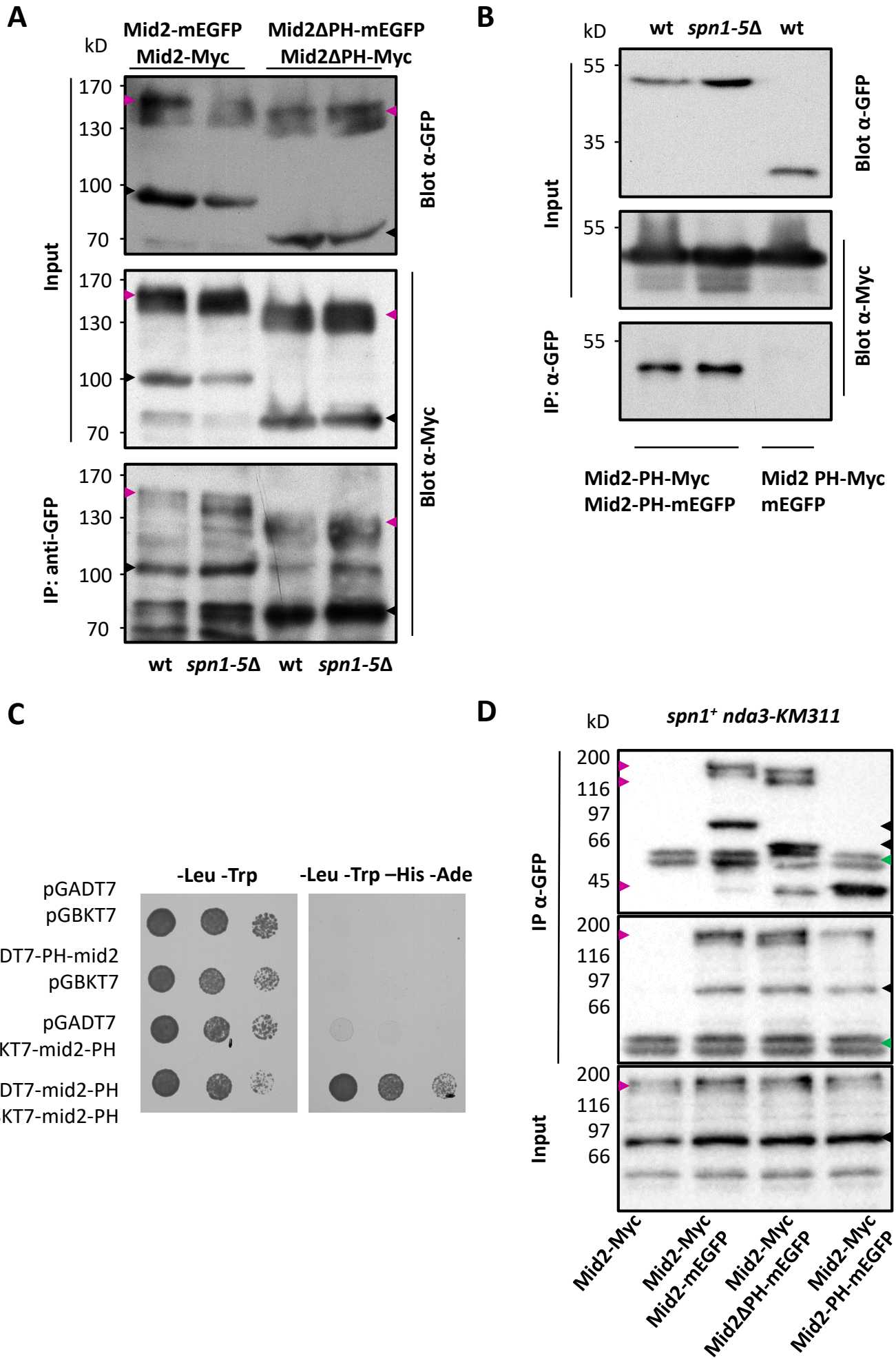
A
kD
Mid2-mEGFP
Mid2-Myc
Mid2ΔPH-mEGFP
Mid2ΔPH-Myc
170
130
100
70
Input
Blot α-GFP
Blot α-Myc
IP: anti-GFP
wt
spn1-5Δ
wt
spn1-5Δ
B
kD
wt
spn1-5Δ
wt
55
35
Input
Blot α-GFP
Blot α-Myc
IP: α-GFP
Mid2-PH-Myc
Mid2-PH-mEGFP
Mid2 PH-Myc
mEGFP
C
-Leu -Trp
-Leu -Trp –His -Ade
pGADT7
pGBKT7
pGADT7-PH-mid2
pGBKT7
pGADT7
pGBKT7-mid2-PH
pGADT7-mid2-PH
pGBKT7-mid2-PH
D
kD
spn1+ nda3-KM311
200
116
97
66
45
IP α-GFP
Blot α-GFP
Blot α-Myc
Input
Mid2-Myc
Mid2-Myc
Mid2-mEGFP
Mid2-Myc
Mid2ΔPH-mEGFP
Mid2-Myc
Mid2-PH-mEGFP

Figure S2

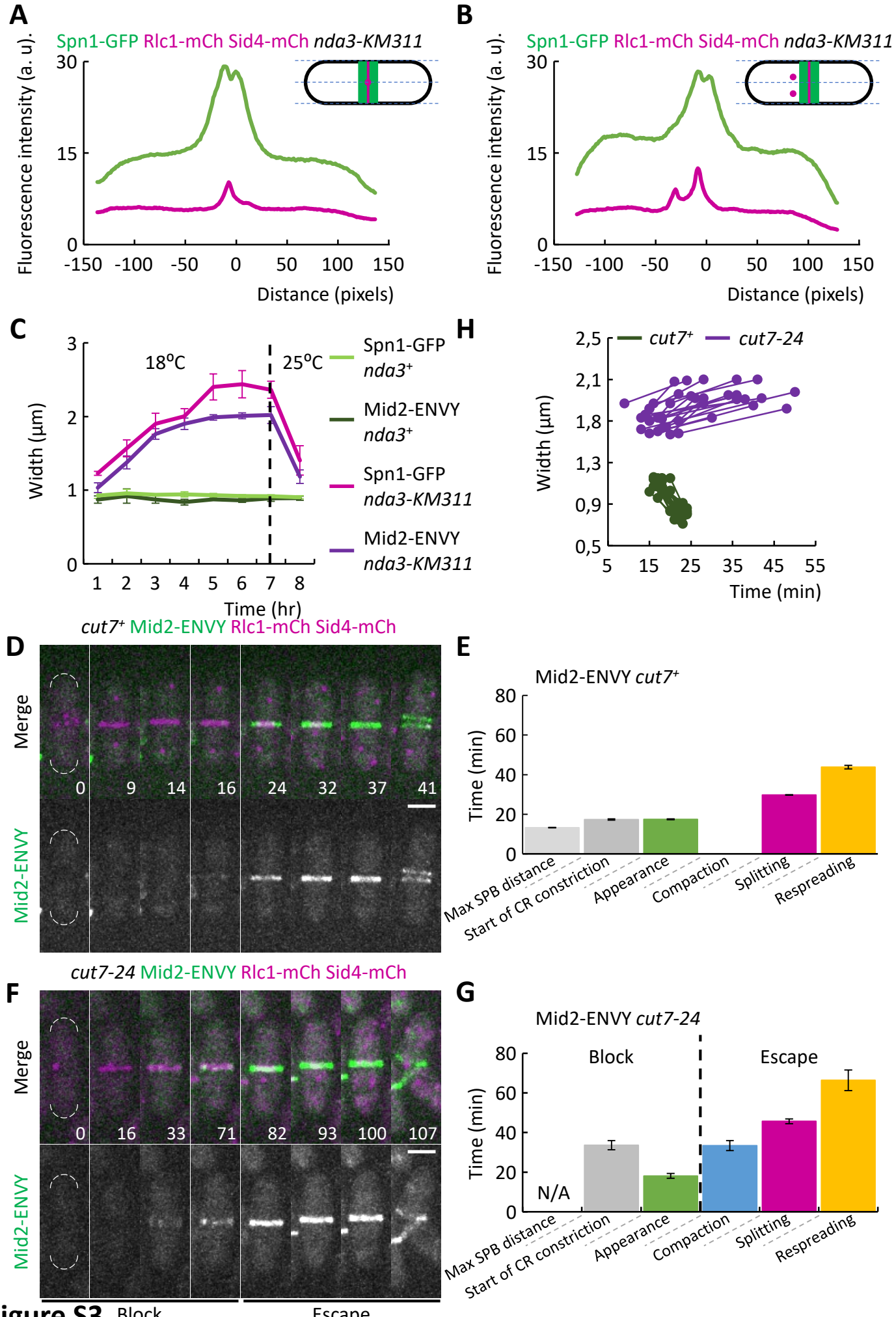
A
Spn1-GFP Rlc1-mCh Sid4-mCh nda3-KM311
Fluorescence intensity (a. u.)
Distance (pixels)
B
Spn1-GFP Rlc1-mCh Sid4-mCh nda3-KM311
Fluorescence intensity (a. u.)
Distance (pixels)
C
18°C
25°C
Width (µm)
Time (hr)
Spn1-GFP nda3+
Mid2-ENVY nda3+
Spn1-GFP nda3-KM311
Mid2-ENVY nda3-KM311
H
cut7+
cut7-24
Width (µm)
Time (min)
cut7+ Mid2-ENVY Rlc1-mCh Sid4-mCh
D
Merge
Mid2-ENVY
0 9 14 16 24 32 37 41
E
Mid2-ENVY cut7+
Time (min)
Max SPB distance
Start of CR constriction
Appearance
Compaction
Splitting
Respreading
cut7-24 Mid2-ENVY Rlc1-mCh Sid4-mCh
F
Merge
Mid2-ENVY
0 16 33 71 82 93 100 107
Block
Escape
G
Mid2-ENVY cut7-24
Block
Escape
N/A
Time (min)
Max SPB distance
Start of CR constriction
Appearance
Compaction
Splitting
Respreading

Figure S3

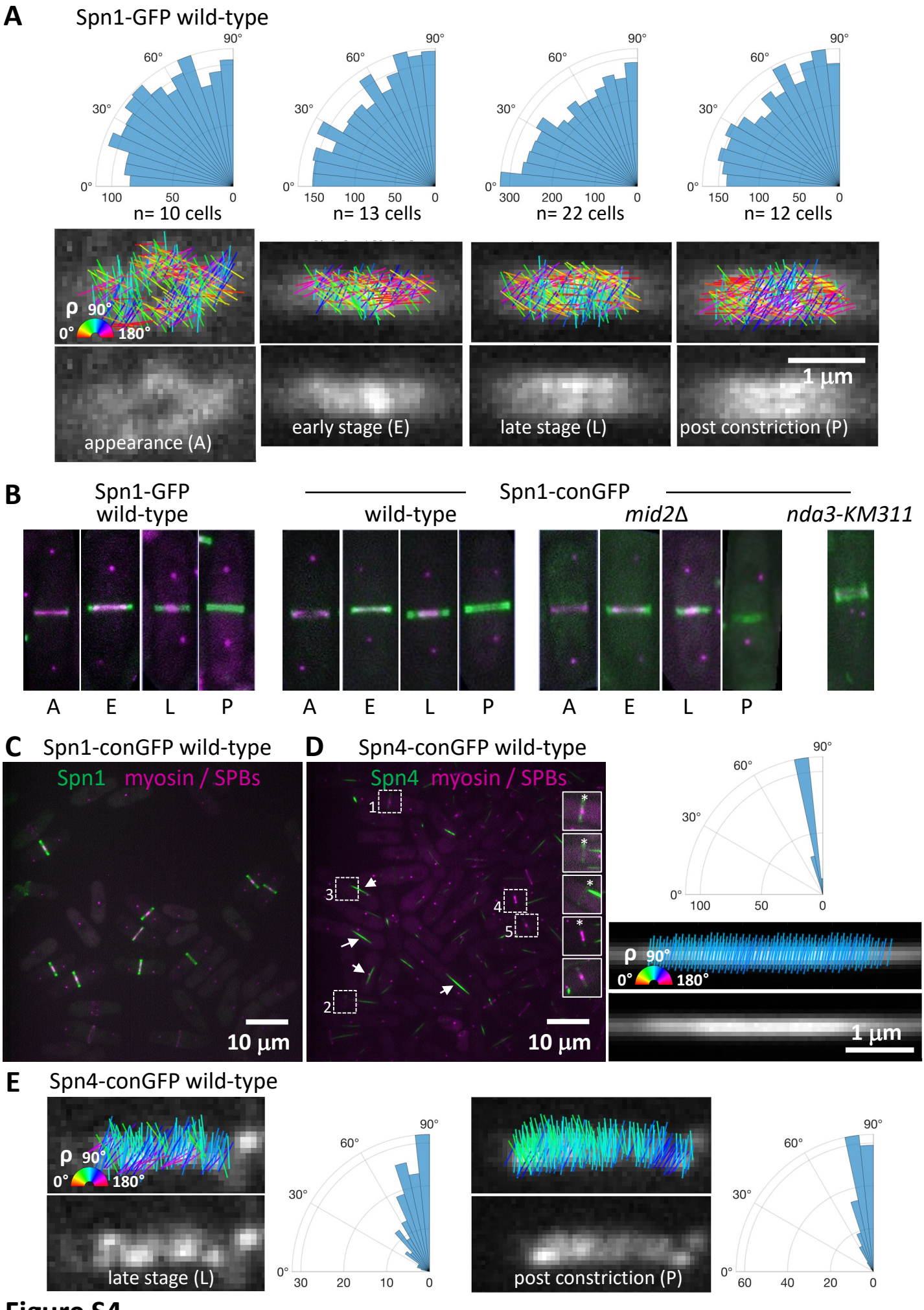
A
Spn1-GFP wild-type
n= 10 cells
n= 13 cells
n= 22 cells
n= 12 cells
ρ 90°
0° 180°
appearance (A)
early stage (E)
late stage (L)
post constriction (P)
1 μm
B
Spn1-GFP wild-type
Spn1-conGFP
wild-type
mid2Δ
nda3-KM311
A E L P
C
Spn1-conGFP wild-type
Spn1 myosin / SPBs
10 μm
D
Spn4-conGFP wild-type
Spn4 myosin / SPBs
1
2
3
4
5
10 μm
1 μm
E
Spn4-conGFP wild-type
late stage (L)
post constriction (P)

Figure S4

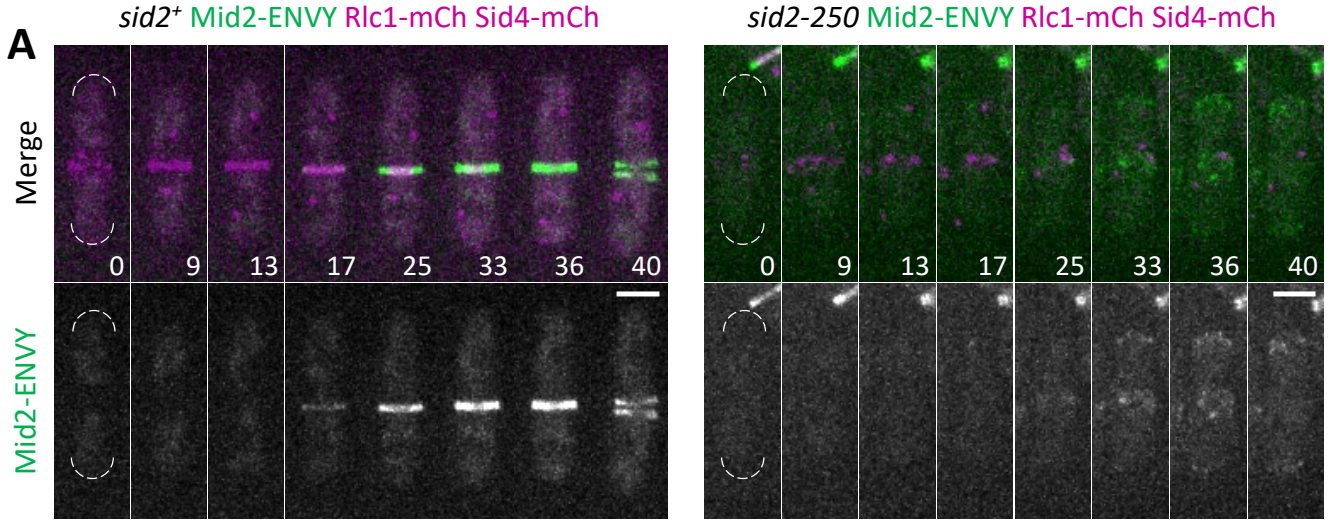
A
sid2+ Mid2-ENVY Rlc1-mCh Sid4-mCh
sid2-250 Mid2-ENVY Rlc1-mCh Sid4-mCh
Merge
Mid2-ENVY
0 9 13 17 25 33 36 40
0 9 13 17 25 33 36 40

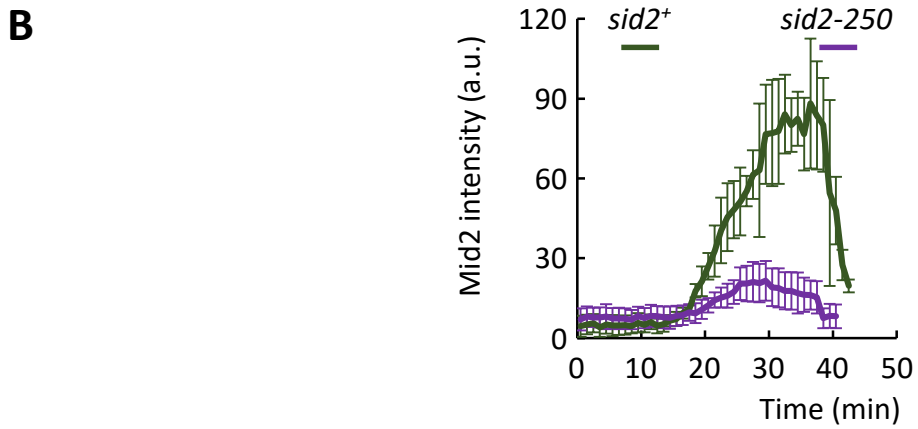
B
sid2+
sid2-250
Mid2 intensity (a.u.)
120
90
60
30
0
0 10 20 30 40 50
Time (min)

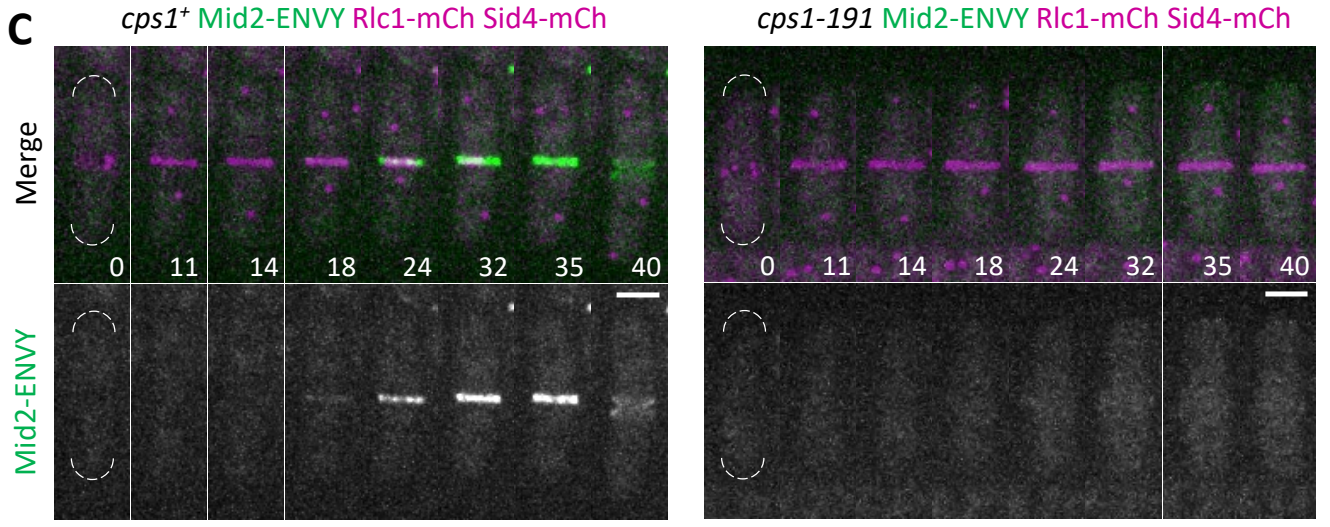
C
cps1+ Mid2-ENVY Rlc1-mCh Sid4-mCh
cps1-191 Mid2-ENVY Rlc1-mCh Sid4-mCh
Merge
Mid2-ENVY
0 11 14 18 24 32 35 40
0 11 14 18 24 32 35 40

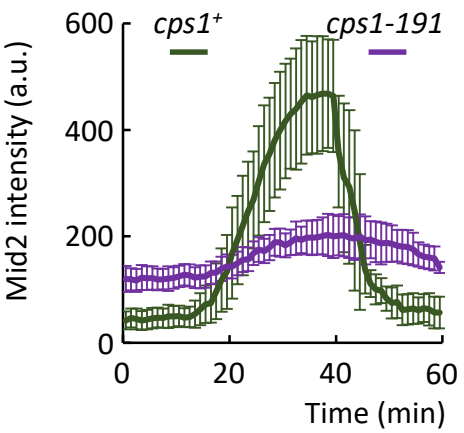
D
cps1+
cps1-191
Mid2 intensity (a.u.)
600
400
200
0
0 20 40 60
Time (min)

Figure S5